The Distribution of Clay Minerals and Their Impact on Diagenesis in Glen Torridon, Gale Crater, Mars

A. Rudolph, B. Horgan, J. Johnson, K. Bennett, J. Haber, J. F. Bell, V. Fox, S. Jacob, S. Maurice, E. Rampe, et al.

▶ **To cite this version:**

A. Rudolph, B. Horgan, J. Johnson, K. Bennett, J. Haber, et al.. The Distribution of Clay Minerals and Their Impact on Diagenesis in Glen Torridon, Gale Crater, Mars. Journal of Geophysical Research. Planets, 2022, 127, 10.1029/2021JE007098 . insu-03867381

HAL Id: insu-03867381

https://insu.hal.science/insu-03867381

Submitted on 12 Apr 2023

HAL is a multi-disciplinary open access archive for the deposit and dissemination of scientific research documents, whether they are published or not. The documents may come from teaching and research institutions in France or abroad, or from public or private research centers.

L'archive ouverte pluridisciplinaire **HAL**, est destinée au dépôt et à la diffusion de documents scientifiques de niveau recherche, publiés ou non, émanant des établissements d'enseignement et de recherche français ou étrangers, des laboratoires publics ou privés.

Distributed under a Creative Commons Attribution - ShareAlike 4.0 International License

Check for updates

JGR Planets

RESEARCH ARTICLE
10.1029/2021JE007098

Special Section:
The Curiosity rover's investigation of Glen Torridon and the surrounding area

The Distribution of Clay Minerals and Their Impact on Diagenesis in Glen Torridon, Gale Crater, Mars

A. Rudolph[1], B. Horgan[1], J. Johnson[2], K. Bennett[3], J. Haber[1], J. F. Bell III[4], V. Fox[5], S. Jacob[4], S. Maurice[6], E. Rampe[7], M. Rice[8], C. Seeger[5], and R. Wiens[1,9]

[1]Purdue University, West Lafayette, IN, USA, [2]Applied Physics Laboratory, Johns Hopkins University, Laurel, MD, USA, [3]U.S. Geological Survey, Astrogeology Science Center, Flagstaff, AZ, USA, [4]Arizona State University, Tempe, AZ, USA, [5]California Institute of Technology, Pasadena, CA, USA, [6]L'Institut de Recherche en Astrophysique et Planetologie, Toulouse, France, [7]NASA Johnson Space Center, Houston, TX, USA, [8]Western Washington University, Bellingham, WA, USA, [9]Los Alamos National Laboratory, Los Alamos, NM, USA

Abstract Glen Torridon (GT) is a recessive-trough feature on the northwestern slope of "Mt. Sharp" in Gale crater, Mars with the highest Fe-/Mg-phyllosilicates abundances detected by the Curiosity rover to date. Understanding the origin of these clay minerals and their relationship with diagenetic processes is critical for reconstructing the nature and habitability of past surface and subsurface environments in Gale crater. We aim to constrain the distribution and extent of diagenesis using compositional and morphological trends observed by visible-to-near infrared reflectance spectra in GT from Mastcam and ChemCam, supported by high-resolution images from the Mars Hand Lens Imager. Spectral features consistent with nontronite and fine-grained red hematite are ubiquitous throughout lower GT, and are strongest where diagenetic features are limited, suggesting that both were formed early, before burial. Diagenetic features increase in both abundance and diversity farther up-section, and we observe morphologic evidence for multiple episodes of diagenesis, with the edge of a diagenetic front partially preserved in the middle stratigraphic member, Knockfarril Hill. Near the contact between GT and the overlying Greenheugh pediment capping unit, we observe a lack of clay minerals with signatures consistent instead with coarse-grained gray hematite, likely formed through late-diagenetic alteration. We hypothesize that the sandstone-dominant Stimson formation acted as a conduit for diagenetic fluid flow into the area and that the clay-rich impermeable GT slowed the flow of those fluids, leading to enhanced alteration surrounding the clay-rich portions of GT, including within the nearby Vera Rubin ridge.

Plain Language Summary The clay mineral-rich region of Glen Torridon on Mt. Sharp provides information to reconstruct the past habitability of the ancient lake environment in Gale crater. Clay minerals have a unique structure that allow for organic matter to be preserved, so regions with high concentrations of clay minerals are of interest for planetary exploration. We use data from the Mastcam cameras, Chemistry and Camera instrument, and Mars Hand Lens Imager on the Mars Science Laboratory *Curiosity* rover to search for trends in rock composition and visual properties to investigate how they have been altered by surface and subsurface water over time. This work has shown that regions with high clay mineral abundances restrict groundwater from penetrating deep into rock units, helping preserve remnants of the early environments where the clay minerals formed, some remnants are exposed on the modern-day surface. Additionally, we observe textural evidence, supported by inferred compositions from spectral data that multiple water-rock interactions led to enhanced alteration and destruction of clay-minerals along the edges of the clay-rich regions. This suggests that there has been a complex history of water-rock interactions in Gale crater, but that regions with high abundances of clay-minerals may still have preserved signs of life.

Key Points:

- Glen Torridon exhibits spectral signatures consistent with Fe-bearing clay minerals and fine-grained red hematite within all members
- The Hutton interval, on the uppermost edge of Glen Torridon, has no clay mineral spectral signatures and instead shows evidence of hematite coarsening
- Clay minerals and fine-grained hematite formed via early weathering and oxidation while coarse-grained hematite formed via late diagenesis

Supporting Information:

Supporting Information may be found in the online version of this article.

Correspondence to:

A. Rudolph,
rudolph4@purdue.edu

Citation:

Rudolph, A., Horgan, B., Johnson, J., Bennett, K., Haber, J., Bell, J. F. III., et al. (2022). The distribution of clay minerals and their impact on diagenesis in Glen Torridon, Gale crater, Mars. *Journal of Geophysical Research: Planets*, *127*, e2021JE007098. https://doi.org/10.1029/2021JE007098

Received 19 OCT 2021
Accepted 12 MAY 2022

© 2022 The Authors.
This is an open access article under the terms of the Creative Commons Attribution-NonCommercial License, which permits use, distribution and reproduction in any medium, provided the original work is properly cited and is not used for commercial purposes.

1. Introduction

Clay minerals have been used as a key indicator of past habitable environments on Mars, as their formation requires prolonged contact with liquid water and their unique sheet-like mineral structure can help preserve biosignatures in the sedimentary record (e.g., Summons et al., 2011; Velde, 1995; Wattel-Koekkoek et al., 2003). Clay minerals can be emplaced through a variety of processes, including in-place surface weathering, authigenic formation in subaqueous environments, detrital transport from other locations, or by ambient or hydrothermal groundwater (e.g., Deocampo, 2015; Ehlmann et al., 2011; Ketzer et al., 1999; McKinley et al., 2002). These

alteration processes can occur over a wide range of pH, water availability, and temperature, all of which can be constrained by analyzing the mineralogy and chemistry of their host rocks (e.g., Deocampo, 2015).

An overarching goal of the Mars Science Laboratory (MSL) mission is to assess the habitability and biosignature preservation potential of ancient Mars, as preserved in the rock record of ancient aqueous environments (Grotzinger et al., 2012). Gale crater was chosen as the landing site for the *Curiosity* rover on the MSL mission based on widespread detections of smectite clays from orbit (Fraeman et al., 2013, 2016; Milliken et al., 2010). The presence of these clay minerals has been confirmed by the Chemistry and Mineralogy (CheMin) X-ray diffractometer onboard MSL, at abundances up to 34 wt.% of the crystalline component in all fluvial and lacustrine sediment samples acquired to date in Gale crater (Bristow et al., 2015, 2018; Rampe et al., 2017; Rampe, Blake, et al., 2020; Rampe, Bristow, et al., 2020; Thorpe et al., 2022). Both the orbital and CheMin data suggest that the clay minerals are dominated by smectites, but their formation mechanism is poorly constrained (e.g., Fraeman et al., 2016; Milliken et al., 2010; Rampe et al., 2017).

Curiosity arrived at the recessive trough feature on Mt. Sharp known as Glen Torridon (GT; Figure 1) in 2019 on sol 2300 (Bennett et al., 2022), which exhibits the strongest clay mineral signatures on Mt. Sharp in orbital short-wave infrared (SWIR; 1.0–2.6 μm) spectra (Fraeman et al., 2016; Milliken et al., 2010). However, the specific environmental implications of clay minerals are difficult to resolve using orbital data alone. Determining the cause of the orbital clay mineral detections in GT, the aqueous history of the unit, and the unit's relationship with surrounding stratigraphic units is critical for understanding the history of water and habitability in Gale crater.

Water activity was not limited to the time around deposition of the sediments that make up Mt. Sharp. MSL data have provided evidence for multiple stages of diagenesis (Bennett et al., 2021; Bristow, Grotzinger, et al., 2021; Fraeman et al., 2020; Frydenvang et al., 2017; Horgan et al., 2020; Kronyak et al., 2019; Nachon et al., 2017; Stack et al., 2014; Sun et al., 2019; Yen et al., 2017), including extensive diagenetic alteration in large, bleached zones on Vera Rubin ridge (VRR), immediately south of GT (David et al., 2020; Horgan et al., 2020; L'Haridon et al., 2020). Bleaching, in this context, means the color-change of bedrock to a lighter tone and does not necessarily imply a specific process.

In this study, we investigate the distribution of clay minerals in GT and their relationship with diagenetic features and locations with inferred late-stage fluid flow. Comparing the distribution of clay minerals and other alteration minerals (e.g., Fe-oxides, sulfates) in GT to the local sedimentology and the distribution of diagenetic features will help constrain the timing and physical extent of diagenetic events. We use color images and visible/near-infrared (VNIR; 447–1,013 nm) multispectral data from the Mast Camera (Mastcam) imaging system on MSL (Bell et al., 2017; Malin et al., 2017), visible (400–840 nm) hyperspectral data from the Chemistry and Camera (ChemCam) spectrometer (Johnson et al., 2015), and color images from the Mars Hand Lens Imager (MAHLI) to evaluate the composition and characterize the morphology of the bedrock in GT. We seek to constrain the extent and timing of diagenetic alteration to test hypotheses regarding why there are more clay minerals present in recessive GT strata relative to the surrounding erosion-resistant regions. These results will contribute to our understanding of the aqueous history in Gale crater and has implications for habitability and preservation of biosignatures in Mt. Sharp.

2. Background

2.1. Mt. Sharp Stratigraphy

Curiosity has traversed through hundreds of meters of fluvial and lacustrine sedimentary strata on the crater floor and on Aeolis Mons (informally known as "Mt. Sharp"), which were likely deposited in the early Hesperian (~3.6 Ga; Fraeman et al., 2016; Milliken et al., 2010). Mt. Sharp resides in the center of Gale crater and is composed primarily of sedimentary rock layers with an approximate total thickness of 5 km (Milliken et al., 2010). Orbital VNIR and SWIR spectral signatures of lower Mt. Sharp transition from clay minerals and Fe-oxides at lower elevations to sulfate minerals at higher elevations (Milliken et al., 2010). This transition is colloquially known as the "clay-sulfate transition" and has been proposed to mark a change from a depositional environment that favored the formation of clay minerals to one that favored the formation of sulfate minerals during the formation of Mt. Sharp (Milliken et al., 2010). As of September 2021, *Curiosity* has explored the clay-dominant regions of Mt. Sharp and is currently studying the clay-sulfate transition.

21699100, 2022, 10, Downloaded from https://agupubs.onlinelibrary.wiley.com/doi/10.1029/2021JE007098 by Cochrane France, Wiley Online Library on [12/04/2023]. See the Terms and Conditions (https://onlinelibrary.wiley.com/terms-and-conditions) on Wiley Online Library for rules of use; OA articles are governed by the applicable Creative Commons License

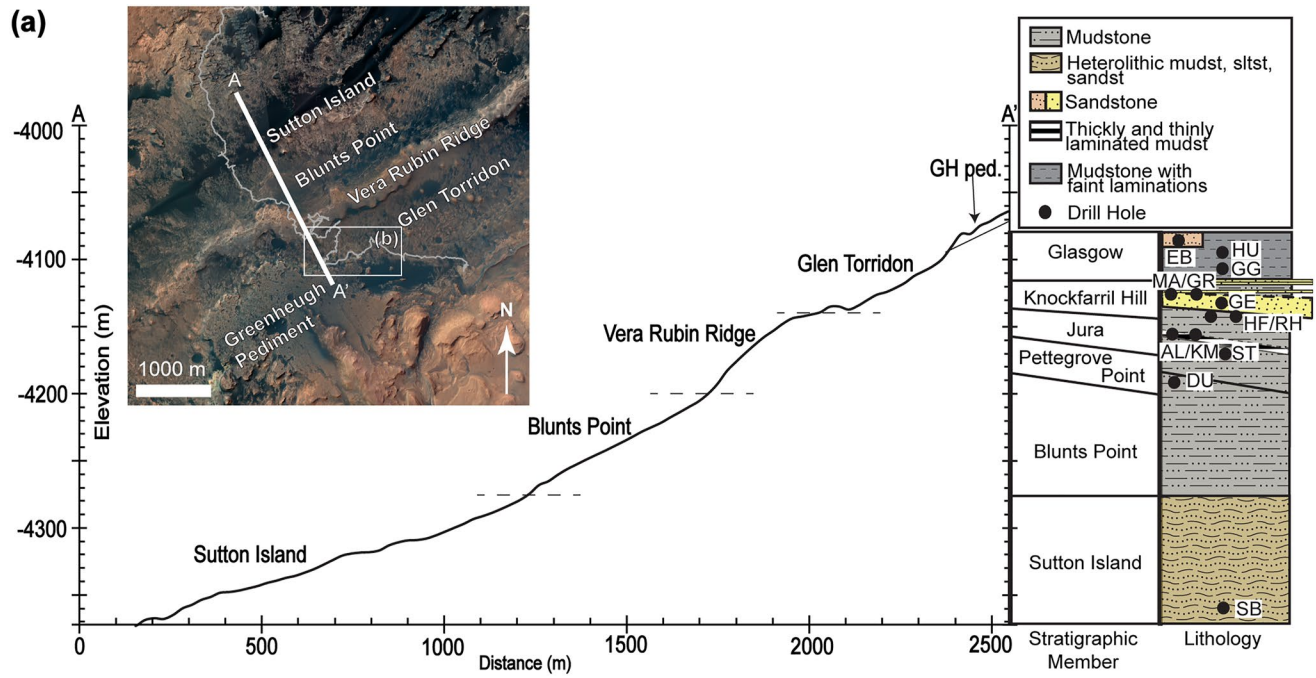

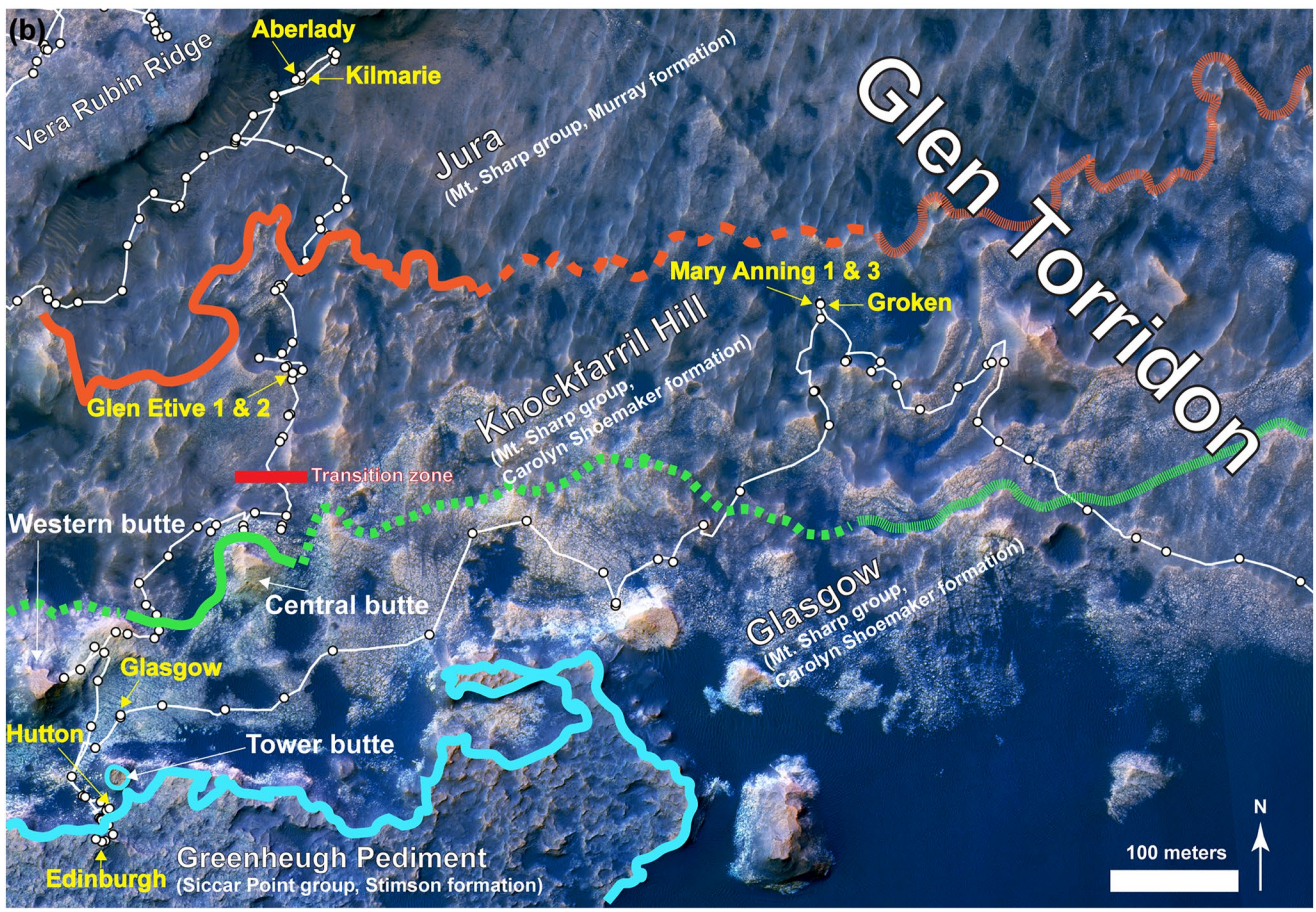

Figure 1.

21699100, 2022, 10, Downloaded from https://agupubs.onlinelibrary.wiley.com/doi/10.1029/2021JE007098 by Cochrane France, Wiley Online Library on [12/04/2023]. See the Terms and Conditions (https://onlinelibrary.wiley.com/terms-and-conditions) on Wiley Online Library for rules of use; OA articles are governed by the applicable Creative Commons License

21699100, 2022, 10, Downloaded from https://agupubs.onlinelibrary.wiley.com/doi/10.1029/2021JE007098 by Cochrane France, Wiley Online Library on [12/04/2023]. See the Terms and Conditions (https://onlinelibrary.wiley.com/terms-and-conditions) on Wiley Online Library for rules of use; OA articles are governed by the applicable Creative Commons License

Three stratigraphic groups have been encountered thus far in *Curiosity's* traverse, the Bradbury group, the Mt. Sharp group, and the Siccar Point group (Fraeman et al., 2016; Grotzinger et al., 2015). The Bradbury group comprises minimally altered detrital fluvio-lacustrine rocks of a mafic composition on the floor of Gale crater (Siebach et al., 2017). The Mt. Sharp group includes the Murray formation (Mf), a >400 m thick package of lacustrine mudstones and sandstones (Grotzinger et al., 2015) and the Carolyn Shoemaker formation (CSf), which is dominated by fine-to medium-grained fluvio-lacustrine sandstones (Fedo et al., 2020, 2022). Each formation is divided into stratigraphic members, differentiated by minor facies changes. Mf members discussed in this work include Sutton Island (SI) which is below VRR, Blunts Point and Pettegrove Point which are both near to or part of VRR, and Jura (Jm) which extends across the landforms of both VRR and GT. CSf members include Knockfarril Hill (KHm) and Glasgow (Gm) which are both within GT. All members in GT (excluding Gm whose grain size has yet to be confirmed at the time of submission) are composed of grains ranging in size from mudstone to sandstone (Minitti et al., 2021; Rivera-Hernández, Sumner, Mangold, et al., 2020; Rivera-Hernández, Sumner, Minitti, et al., 2020). The bulk mineralogy of the Mf derived from CheMin data includes variable amounts of feldspars, phyllosilicates, hematite, jarosite, pyroxene, olivine, X-ray amorphous materials, magnetite, and other minor constituents (Rampe et al., 2017; Rampe, Blake, et al., 2020).

The Siccar Point group (SPg) is an aeolian sandstone capping unit that unconformably overlies the Mt. Sharp group and includes the Stimson formation (Banham et al., 2018; Fraeman et al., 2016). The Stimson formation has been observed at multiple elevations along the rover traverse and is comprised of heterolithic sandstones with a dominant mafic composition similar to the Bradbury group (Bedford et al., 2020). At the Greenheugh (GH) pediment the Stimson formation overlies the Glasgow member of GT and includes sandstone and mudstone with a minimally altered mafic composition (Banham et al., 2020, 2022; Bedford et al., 2021, 2022).

2.2. Glen Torridon

This paper focuses on the GT region of Mt. Sharp. GT is a local topographic low with trough-like morphology that stretches, on its short axis, ∼500 m in the NNW/SSE direction. GT is bounded by two erosion-resistant units, VRR to the north and the GH pediment to the south (Figure 1). Three stratigraphic members outcrop within GT (Fedo et al., 2020, 2022), in order of increasing elevation: (a) Jura, (b) Knockfarril Hill, and (c) Glasgow (Figures 1b and 2). The Jm is a part of the Mf and is characterized by thinly laminated mudstones with minor sandstone components (Minitti et al., 2021; Rivera-Hernández, Sumner, Mangold, et al., 2020; Rivera-Hernández, Sumner, Minitti, et al., 2020). In this manuscript we focus on the part of the Jm that outcrops in GT, which we refer to as the GT Jm. Because the Jm outcrops in both VRR and GT, at times at the same elevation, this implies that at least portions of GT and VRR were deposited contemporaneously. However, the mineralogy and distribution of diagenetic features differs greatly between the Jm rocks that outcrop in VRR and those that outcrop in GT (e.g., Edgar et al., 2020; Horgan et al., 2020). The KHm is the first stratigraphic member encountered in the CSf and is characterized by fractured bedrock with interstratified mudstones and sandstones, often observed as a capping unit on buttes near VRR and within the lower stratigraphy of buttes in southeastern GT (Western, Central, and Tower buttes; Figure 1b). The Gm is within the CSf and is characterized by light-toned, highly fractured, and finely laminated bedrock (Bennett et al., 2022; Fedo et al., 2020, 2022; Fox et al., 2020).

GT was previously known as the "clay-bearing unit" based on previously mentioned orbital detections of Fe/Mg-smectites (Fraeman et al., 2016; Milliken et al., 2010). Absorption bands centered at 1.9 μm and ∼2.2–2.3 μm are observed that are consistent with smectite clays (Fraeman et al., 2016). While lower Mf stratigraphy shows variable band positions consistent with Al/Mg/Fe-bearing smectites (Bristow et al., 2015), the band position in GT is consistently near 2.29 μm, indicating nontronite (Fe^{3+}-rich smectite; Czarnecki et al., 2020, 2022).

Figure 1. Context of Glen Torridon within Mt. Sharp. (a) Cross-section A-A' from Sutton Island to the Greenheugh pediment along with equivalent portion of the stratigraphic column along *Curiosity's* traverse (Fedo et al., 2020, 2022), location shown on inset over HiRISE color mosaic (HiRISE images ESP_053732_1750 and ESP_061961_1750). Drill hole targets shown in stratigraphic column and in Figure 1b use the following acronyms: Aberlady (AB), Kilmarie (KM), Glen Etive 1 and 2 (GE 1 and 2), Hutton (HU), Edinburgh (EB), Glasgow (GG), Mary Anning 1 and 3 (MA 1 and 3), and Groken (GR). (b) HiRISE false-color image of Glen Torridon (HiRISE images ESP_053732_1750 and ESP_061961_1750). Landforms and stratigraphic members are labeled in white and drill sites are labeled in yellow. *Curiosity's* traverse is denoted by a white line and approximate boundaries between stratigraphic members are denoted by orange, green, and blue lines. Solid lines are confident boundaries; dashed lines indicate relative degree of certainty where the more frequent the dashes, the higher the uncertainty. The bold red line denotes a transition zone in Knockfarril Hill that may record a diagenetic front (see Section 4).

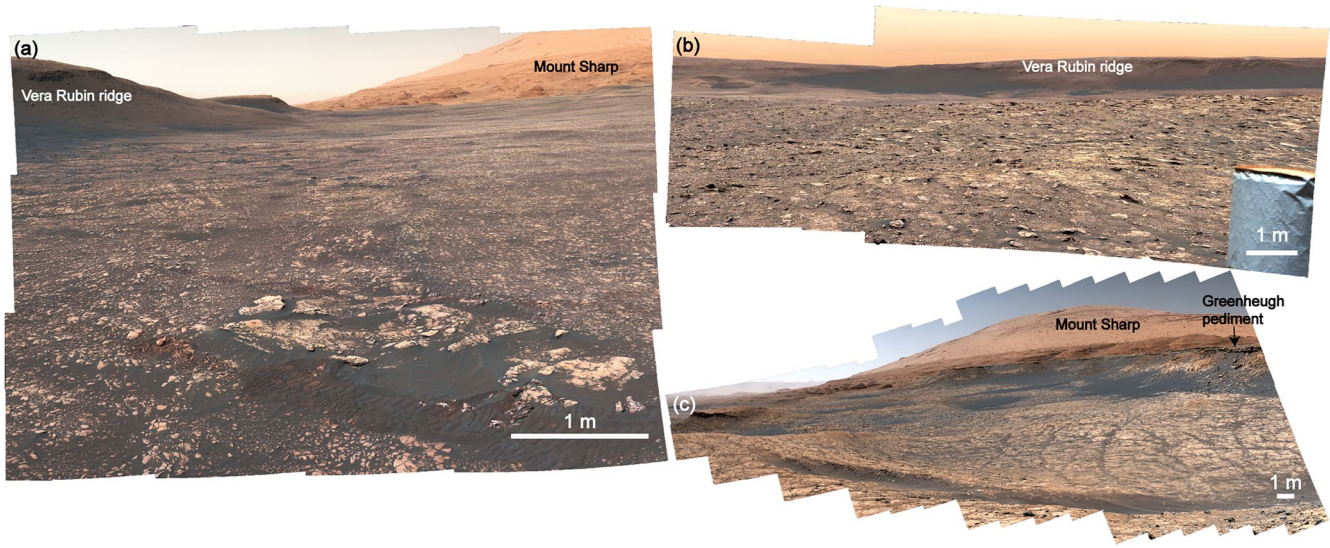

Figure 2. Mastcam enhanced color mosaics representing the three stratigraphic members in Glen Torridon (GT). All three members exhibit flat-lying, recessive textures relative to Vera Rubin ridge and Greenheugh pediment. (a) GT Jura member comprised primarily of rubbly bedrock with very few defined fractures, L0 (Bayer filters) mcam012780 on Sol 2411. (b) Knockfarril Hill member comprised of more coherent bedrock, L0 (Bayer filters) amcam014877 on Sol 2845. (c) Glasgow member comprised of coherent bedrock with large fractures observed within the bedrock, R0 (Bayer filters) mcam013827 on Sol 2641.

These orbital clay detections have been confirmed upon *Curiosity's* exploration of Mt. Sharp and GT. XRD patterns and evolved H_2O detected by the Sample Analysis at Mars (SAM) gas chromatograph mass spectrometer indicate that most clay minerals are dehydrated smectite (i.e., lacking interlayer H_2O; McAdam et al., 2020; Rampe, Bristow, et al., 2020; Sutter et al., 2017). There is a gradual change in smectite composition within the Mf strata, from Mg^{2+}/Fe^{2+}-bearing trioctahedral smectite at the base of the section to Al^{3+}/Fe^{3+}-bearing dioctahedral smectite going up-section and into GT (Bristow et al., 2018). Some drill targets in Gale crater show evidence for other phyllosilicates in addition to dehydrated smectite. Expanded smectite is present at the base of the section (Vaniman et al., 2014), a ferripyrophyllite-like phase was identified near the base of the Mf and in VRR (Achilles et al., 2020; Bristow et al., 2018; Rampe, Bristow, et al., 2020), and a mixed-layer serpentine-talc may be present in GT (e.g., Bristow, Grotzinger, et al., 2021). CheMin and SAM analyses suggest that the specific clay minerals observed in GT are primarily collapsed dioctahedral Fe^{3+}-bearing smectite (i.e., nontronite), with possible minor amounts of mixed-layer serpentine-talc, consistent with orbital nontronite detections. Other minerals detected by CheMin in GT include plagioclase, pyroxene, sanidine, anhydrite, bassanite, quartz, cristobalite, hematite, magnetite, siderite, and fluorapatite. X-ray amorphous material is also abundant in every drill target (Bristow, Grotzinger, et al., 2021; Thorpe et al., 2020, 2022).

GT is the first place on Mt. Sharp where MSL has investigated a clay mineral deposit that was originally observed from orbit (Milliken et al., 2010) and has provided an opportunity to constrain clay mineral formation processes on Mars. Some clay mineral formation mechanisms that have been proposed globally on Mars include lakes (e.g., Bibring et al., 2006; Ehlmann et al., 2008; Hurowitz et al., 2017; Rampe et al., 2017), pedogenesis (e.g., Bibring et al., 2006; Bishop et al., 2018; Carter et al., 2015; Noe Dobrea et al., 2010), hydrothermal environments (e.g., Arvidson et al., 2014; Ehlmann et al., 2011; Newsom, 1980), subsurface diagenesis (Ehlmann et al., 2011; Michalski et al., 2013), and under a dense, steamy atmosphere (Cannon et al., 2017). Within the Mf, the proposed origin of the clay minerals has evolved as the mineralogy and context of the clays has changed with elevation (Hurowitz et al., 2017; Rampe et al., 2017). It has been inferred that Mg-bearing trioctahedral smectites at the base of the section formed in a closed-system shortly after sediment deposition in a lacustrine environment (Bristow et al., 2018; Rampe, Bristow, et al., 2020; Treiman et al., 2014; Vaniman et al., 2014). In contrast, Fe/Al-bearing dioctahedral smectites may have formed through surface weathering, either in the catchment, during transport, or within the lake sediments (Bristow et al., 2018; Rampe, Bristow, et al., 2020). The ferripyrophyllite-like phase may have formed during diagenesis at slightly elevated temperatures or may be detrital (Bristow et al., 2018; Rampe, Bristow, et al., 2020). The possible serpentine-talc is likely detrital and sourced from serpentinized ultramafic rocks (Bristow, Grotzinger, et al., 2021).

21699100, 2022, 10, Downloaded from https://agupubs.onlinelibrary.wiley.com/doi/10.1029/2021JE007098 by Cochrane France, Wiley Online Library on [12/04/2023]. See the Terms and Conditions (https://onlinelibrary.wiley.com/terms-and-conditions) on Wiley Online Library for rules of use; OA articles are governed by the applicable Creative Commons License

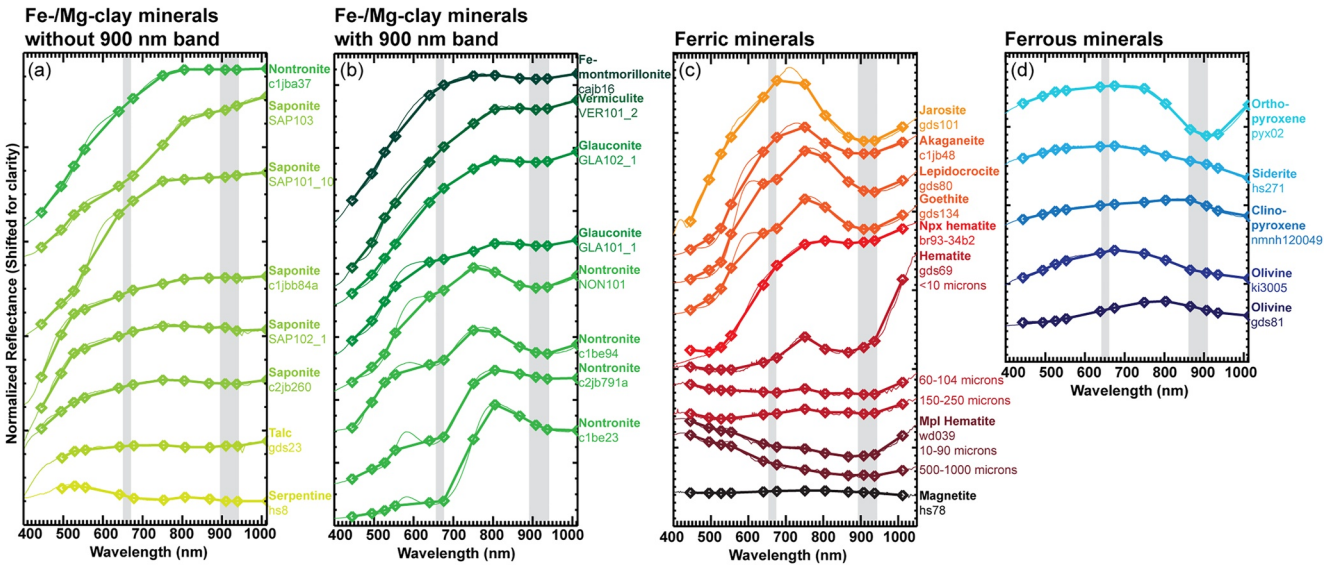

Figure 3. Laboratory reference spectra. (a) Fe-/Mg-clay minerals that lack a ≥ 900 nm absorption band, (b) Fe-/Mg-clay minerals that have a ≥ 900 nm absorption band, (c) ferric minerals that exhibit an absorption band centered near ~670 nm and/or ≥ 900 nm, and (d) ferrous minerals that have a ≥ 900 nm absorption band. Key Fe/Mg-clay absorption bands (650–670 nm and 900–950 nm) are indicated by light gray boxes on each plot. Lab spectra are sourced from the Reflectance Experiment Laboratory (Pieters, 1983), the USGS Spectral Library Version 7 (Kokaly et al., 2017), and the University of Winnipeg's Centre for Terrestrial and Planetary Exploration's spectral database.

This work utilizes the VNIR instrumentation onboard the *Curiosity* rover to map the distribution of Fe^{3+}-bearing clay minerals and Fe^{3+}-oxides within the stratigraphic members of GT to constrain the timing of early and late diagenetic processes in Mt. Sharp. We hypothesize that clay mineral formation in GT occurred during early diagenesis, which may have included some combination of surface and near-surface aqueous alteration in the original lacustrine environment, surface weathering, and pedogenesis. This hypothesis predicts that clay minerals would likely be absent near late-stage diagenetic features (e.g., bleached halos; Bennett et al., 2021). In contrast, they would be associated with features such as fine-grained laminations, alteration rinds, and/or soil horizons that are consistent with early environment processes. To test this hypothesis, we investigate the distribution and correlation of clay minerals and diagenetic features in GT.

3. Methods

MSL has two instruments that are sensitive to reflectance in the VNIR wavelength range: Chemistry and Camera (ChemCam), which collects passive reflectance point spectra (400–840 nm; Johnson et al., 2015, 2016) and Mast Camera (Mastcam), which takes multispectral images (400–1,014 nm; Bell et al., 2017; Malin et al., 2017). Fe-bearing rocks, including Fe-bearing smectites, exhibit absorption bands within this wavelength range (Bishop et al., 2008). Absorptions centered between ~600 and 760 nm are due to $Fe^{2+/3+}$ charge transfer (Anderson & Stucki, 1979; Sherman, 1990), ferric (Fe^{3+}) minerals commonly exhibit an absorption near 900 nm due to spin forbidden transitions in ferric iron (e.g., Hunt, 1977; Morris et al., 1985), and absorptions centered between 900 and 1,300 nm are due to crystal field effects in ferrous (Fe^{2+}) iron minerals (Adams, 1968; Cloutis & Gaffey, 1991; Horgan et al., 2014). Specific spectral features used in this study that are indicative of $Fe^{2+/3+}$-bearing phyllosilicates include an absorption band centered at ~670 nm and an absorption band centered at ≥900 nm (Figure 3b; Anderson & Stucki, 1979; Bishop et al., 2008). However, not all Fe/Mg-phyllosilicates exhibit both diagnostic absorption bands mentioned previously (e.g., saponite; Figure 3a).

Figure 3c shows examples of other relevant minerals that exhibit subtle differences in the wavelength range of Mastcam. Anhydrite exhibits an absorption band centered at ~650 nm but does not exhibit absorption bands beyond 800 nm. Jarosite, akaganeite, lepidochrosite, and goethite can all have absorption bands centered at similar wavelengths to $Fe^{2+/3+}$-bearing phyllosilicates, so differentiating these minerals is reliant on using VNIR spectra in tandem with quantitative datasets (e.g., CheMin, SAM). Hematite has a diagnostic absorption centered near 860 nm that is distinct from clay minerals (Morris et al., 1989) and a strong red-to-blue-ratio (RBR) that

21699100, 2022, 10, Downloaded from https://agupubs.onlinelibrary.wiley.com/doi/10.1029/2021JE007098 by Cochrane France, Wiley Online Library on [12/04/2023]. See the Terms and Conditions (https://onlinelibrary.wiley.com/terms-and-conditions) on Wiley Online Library for rules of use; OA articles are governed by the applicable Creative Commons License

21699100, 2022, 10, Downloaded from https://agupubs.onlinelibrary.wiley.com/doi/10.1029/2021JE007098 by Cochrane France, Wiley Online Library on [12/04/2023]. See the Terms and Conditions (https://onlinelibrary.wiley.com/terms-and-conditions) on Wiley Online Library for rules of use; OA articles are governed by the applicable Creative Commons License

decreases at coarser grain sizes. Magnetite has no notable absorptions in this wavelength range and has a low RBR (i.e., flat spectrum).

Atmospheric dust on Mars accumulates on the bedrock and other undisturbed targets. Dust can strongly influence spectral properties in the VNIR range and causes an increase in overall reflectance and an increase in slope between 400 and 700 nm (Kinch et al., 2015). Some bedrock targets have had the majority of dust removed using the Dust Removal Tool (DRT), and these targets are critical for assessing the effects of dust on Mastcam spectra.

Drill tailings are a good proxy for CheMin samples from those locations, and we use both tailings and pre-drill bedrock spectra in our comparisons to CheMin data. Any differences in spectral features in tailings and surface targets are attributed to changes made because of the drilling process that homogenizes and fines the samples rather than variability between the sub-surface and the surface.

3.1. Mastcam

The Mastcam instrument is a multispectral imager mounted on the remote sensing mast of the *Curiosity* rover ~2 m above the surface (Bell et al., 2017; Wellington et al., 2017). Mastcam consists of two 1,600 × 1,200 pixel Bayer-patterned CCD cameras at fixed focal lengths of 100 mm for the right camera (M100) and 34 mm for the left camera (M34; Bell et al., 2017). These cameras capture multispectral image sets with three wide-band Bayer filters, corresponding to red, green, and blue wavelengths, and nine narrow-band filters (Table S1 in Supporting Information S1) spread across both cameras in the VNIR range (445–1,013 nm; Bell et al., 2017; Malin et al., 2017; Wellington et al., 2017). The accuracy of Mastcam spectral data is <±10% based on pre-flight radiometric calibration coefficient calculations and the filter-to-filter precision is <±7% (Bell et al., 2017). Raw Mastcam data are converted from digital number (DN) values to irradiance (W/m^2), and then to radiance (W/m^2/nm/sr) using preflight calibration measurements, as described by Bell et al. (2017). A calibration target on the deck of the rover is imaged along with each multispectral image set, and spectra from the calibration target are used to model the effects of illumination and viewing geometry as well as atmospheric scattering in Mastcam images and thus convert radiance images into radiance factor (I/F; Bell et al., 2017; Kinch et al., 2015; Wellington et al., 2017).

In this study, we examined 62 Mastcam full-filter multispectral image sets acquired between sols 2302 and 2975 that were calibrated to radiance and processed to relative reflectance (I/F). This study specifically focuses on image sets corresponding to all drill sites and targets in which the DRT was used to clear bedrock targets. Targets analyzed in this study are listed in Table S2 in Supporting Information S1. Color diversity was qualitatively evaluated using white-balanced approximate true-color images and enhanced-color stretches applied to Bayer filter images ("R0/L0").

Regions of interest (ROIs) were manually defined first within each higher resolution M100 (right) image to sample the range of spectral diversity within bedrock, diagenetic features, DRT spots, and drill tailings. ROIs of approximately the same areas within the overlapping lower resolution M34 (left) image were then selected. For each ROI in the M34 and M100 images, the reflectance values for each pixel in the ROI were averaged for each filter and the standard deviation was calculated. The M34 and M100 spectra were then combined by scaling the M100 spectra to the M34 spectra at 1,013 nm and averaging overlapping filters. The minimum ROI size is primarily limited by the resolution of the M34 image, which has one-third the resolution of M100. The smallest ROI here contains at least 7 pixels in the M34 image, but typically ROIs are larger (~20–200 pixels; Table S3 in Supporting Information S1). Small ROIs have been manually double checked with each of the individual filter images to confirm that the ROI is consistent between the M100 and M34 images and that there has not been any spatial misregistration between filters. ROIs are selected to emphasize areas with consistent spectral shapes, so standard deviation error bars in Mastcam spectra primarily reflect variability in overall I/F within the ROI. Because of this, ROIs of highly reflective targets often have large error bars in part due to their variable albedo.

Spectral parameters were calculated for all collected spectra, including RBR (red/blue ratio: 676/527 nm) and the 805/640 nm ratio. These parameters are based on previous work in Horgan et al. (2020) and Johnson et al. (2015, 2016). The wavelength position of the ~900 nm band is a useful mineral indicator, and we have parameterized this as both band minimum and band center (Horgan et al., 2014). The ~900 nm band minimum was calculated as the position of the minimum value after continuum removal between 805 and 937 nm (Figure S1 in Supporting Information S1). Band center was calculated as the position of the minimum value of a

21699100, 2022, 10, Downloaded from https://agupubs.onlinelibrary.wiley.com/doi/10.1029/2021JE007098 by Cochrane France, Wiley Online Library on [12/04/2023]. See the Terms and Conditions (https://onlinelibrary.wiley.com/terms-and-conditions) on Wiley Online Library for rules of use; OA articles are governed by the applicable Creative Commons License

higher-resolution second order polynomial fit to this continuum-removed spectrum. Although calculating a band center in this fashion enables comparison to lab spectra of relevant minerals (especially hematite and clays), it is subject to uncertainties on the order of the filter bandpasses (~0.01 μm). Targets whose fit curve in this wavelength range did not produce a convex line (attributed to a lack of an absorption in the non-fit spectrum) were not included as a band center could not be confidently calculated.

3.2. ChemCam

The ChemCam instrument collects single-point passive reflectance spectra between 400 and 840 nm to support laser-induced breakdown spectroscopy (LIBS; Maurice et al., 2012; Wiens et al., 2012). While not the primary function of the ChemCam instrument, the higher spectral resolution of reflectance spectra in this wavelength range relative to Mastcam allows detailed analysis of the position and depth of absorption bands and slopes in the VNIR range, which can be used to constrain $Fe^{2+/3+}$ mineralogy (e.g., Johnson et al., 2015). ChemCam spectra are calibrated by correcting the digital number (DN) for inherent background noise, converting to photons (unit of photons/DN; Wiens et al., 2012) then using the angular field-of-view and distance from the target to calculate the associated area along with the solid angle subtended by the telescope aperture. Radiance values were calculated and converted into standard units ($W/m^2/sr/\mu m$; Johnson et al., 2015). Absolute calibration uncertainty (3-sigma) for the VNIR range of ChemCam spectra is ~6% (Johnson et al., 2015). Multiple spectra were acquired from a single target and averaged to increase signal-to-noise ratio (Johnson et al., 2015). ChemCam targets analyzed in this work correspond to Mastcam multispectral images, with a focus on drill tailings targets (Figure S2 in Supporting Information S1). Band depth at 650 nm was calculated using shoulders at 600 and 700 nm and by averaging reflectance values within 5 nm of the wavelengths of interest to minimize channel-to-channel noise.

3.3. MAHLI

MAHLI is a color camera mounted on the arm of *Curiosity* that captures images of small-scale features (submm-to-cm size) at a resolution ranging from ~17 to ~100 μm/pixel depending on the standoff distance (Edgett et al., 2012; Robinson et al., 2013). MAHLI images taken over the span of the study sol range were qualitatively analyzed to categorize type and relative abundance of diagenetic features observed on bedrock throughout GT (Table S4 in Supporting Information S1).

4. Classification of Diagenetic Features in Glen Torridon

This work categorizes morphology, relative abundance, and distribution of diagenetic features in GT; chemical analyses of specific diagenetic features are presented in Gasda et al. (2021, 2022). Representative images of diagenetic feature categories are shown in Figure 4 and the distribution of diagenetic features in the GT members is summarized in Table 1. Many of these diagenetic feature types have been previously observed in MAHLI images from VRR (Bennett et al., 2021).

Light-toned veins, both cross-cutting and parallel to bedding (Figure 4a) are observed in all GT stratigraphic members. Dark-toned veins are primarily observed cross-cutting bedding in KHm and Gm, but not GT Jm (Figure 4b).

A variety of dark gray features with different morphologies are present in GT bedrock. Dark gray nodules are raised spherical features often observed in clusters on bedrock (Figure 4c), while other dark gray features have no consistent shape (Figure 4d). Dark gray crystal fragments have multiple points radiating out from their center and are only observed in KHm (Figure 4e). We find two types of dark gray circular features: those that are flush with the bedrock surface and show light-toned interiors (Figure 4f) and "casings" that protrude from the surface and have hollow interiors (Figure 4g), and both are only observed in the Gm.

Discoloration (Figure 4h) and bleached halos (Figure 4i) are both circular patches of variable color on bedrock, but bleached halos are small and strictly light-toned with a dark-toned center, while discoloration is broader, encompassing variable color change, including light-toned colors, red and/or gray patches of discoloration.

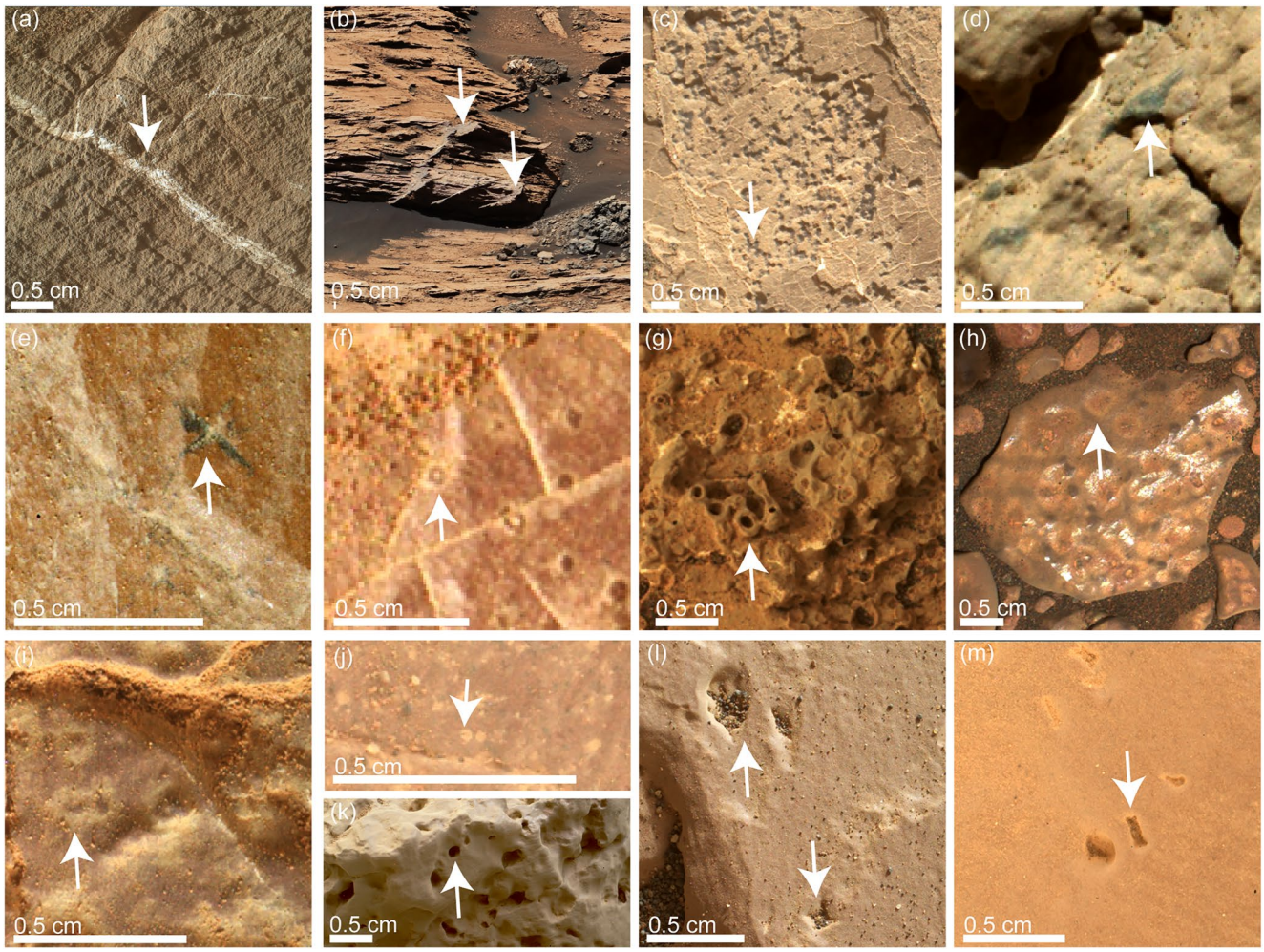

Figure 4. Mars Hand Lens Imager (MAHLI) and Mastcam R0 color images of diagenetic features observed throughout Glen Torridon (NASA/JPL/ASU/MSSS). Specific features are highlighted by the white arrows. (a) Light-toned veins MAHLI sol 2444 Beauly, (b) dark-toned veins, mcam13550 sol 2581 Kinraddie, (c) dark gray nodules, MAHLI sol 2908 Groken, (d) dark gray features, MAHLI sol 2611 Renfrewshire, (e) dark gray crystal fragments, MAHLI sol 2597 Everbay, (f) dark gray circular features with no fill, MAHLI sol 2974 Cod Baa, (g) casings, MAHLI sol 2660 Bogmill Pow, (h) discoloration, MAHLI sol 2972 Torness, (i) bleached halos, MAHLI sol 2792 Hedgeley Moor, (j) small-scale pitting, MAHLI sol 2367 Aberlady, (k) large-scale pitting, MAHLI sol 2564 Pitmedden, (l) star-shaped pits, MAHLI sol 2363 Ardnamurchan, and (m) rectangular pits MAHLI sol 2449 Tolsta.

Pitting is observed as small-scale (Figure 4j) and large-scale circular pits (Figure 4k). Star-shaped (Figure 4l) and rectangular pits (Figure 4m) are both inferred to be former crystal fragments (Bennett et al., 2021).

The GT Jm and the GH pediment exhibit a low density and diversity of diagenetic features compared to the Gm and KHm, which exhibit a wide array of diagenetic features that vary in density and expression with location within the members (Table 1). *Curiosity* first encountered the KHm on sols 2450–2580 and found a relative increase in abundance of diagenetic features around sol 2565; the term "transition zone" is used to denote this boundary (Figure 1). This increase in diagenetic features beyond the transition zone is primarily in the form of the appearance of dark diagenetic features and bedrock discoloration, which are uncommon in lower KHm bedrock. *Curiosity* encountered KHm again from ~sol 2816–2950 after exploring the Gm and GH pediment, and this area also exhibits high abundances of dark diagenetic features.

Bedrock throughout Gm exhibits the greatest number of diagenetic features in GT both in type and overall abundance, and there is also a distinct increase in diagenetic features near the contact of Gm and the GH pediment capping unit. Diagenetic features include a variety of dark gray features and discoloration as observed in upper KHm, and Gm also exhibits the clearest examples of hollow circular features, casings, and bleached halos.

21699100, 2022, 10, Downloaded from https://agupubs.onlinelibrary.wiley.com/doi/10.1029/2021JE007098 by Cochrane France, Wiley Online Library on [12/04/2023]. See the Terms and Conditions (https://onlinelibrary.wiley.com/terms-and-conditions) on Wiley Online Library for rules of use; OA articles are governed by the applicable Creative Commons License

Table 1
Diagenetic Features Observed in Different Regions Within Glen Torridon

Diagenetic Feature		Stratigraphic Member: Glen Torridon Jura Sols 2302 – 2438 (13 images)	Knockfarril Hill: Sols 2439 – 2563 (15 images)	Knockfarril Hill: Sols 2564 – 2580 (10 images)	Knockfarril Hill: Sols 2801 – 2950 (15 images)	Glasgow: Sols 2581– 2801 (38 images)	Glasgow: Sols 2951– 2975 (7 images)	Greenheugh Pediment Sols 2691– 2747 (8 images)
Veins	Light-toned	85%	73%	50%	73%	90%	86%	13%
	Dark-toned		27%	10%		13%		
Dark gray ___	Nodules		7%	30%	27%	61%	86%	75%
	Features			30%	27%	18%	29%	
	Crystal fragments			20%				
	Hollow circular features					3%	14%	
	Casings					3%		
Discoloration	General discoloration	8%		10%	7%	3%	57%	
	Bleached halos					5%		
Pitting	Small-scale	8%						
	Large-scale	8%	20%	20%		3%		
	Star-shaped	15%				3%		
	Rectangular	15%						

Note. Percentage represents how many images in each category have the feature in question. Red line marks the start of "transition zone" in Knockfarril Hill (KHm) (see also Figure 1). See Tables S4 and S5 in Supporting Information S1 for a complete list of Mastcam mosaics and Mars Hand Lens Imager images used here.

Along the contact between the Gm and the GH pediment capping unit, there is a laterally extensive outcrop of light-toned bedrock (Figure 5). This outcrop along the rover traverse is colloquially known as the "Hutton interval", and is visible in both Mastcam and orbital images (Figure 1). This Hutton interval is only observed in the Gm and not in the GH pediment capping unit and is lighter toned than typical Gm bedrock (Figure 2c). The Hutton interval exhibits a somewhat higher abundance of diagenetic features compared to typical Gm and is the only region of GT that has casings (Figure 4g). Light-toned bedrock zones of a similar scale were observed in the previously traversed VRR (Figure 5b) and was proposed to be due to late diagenetic bleaching (Horgan et al., 2020).

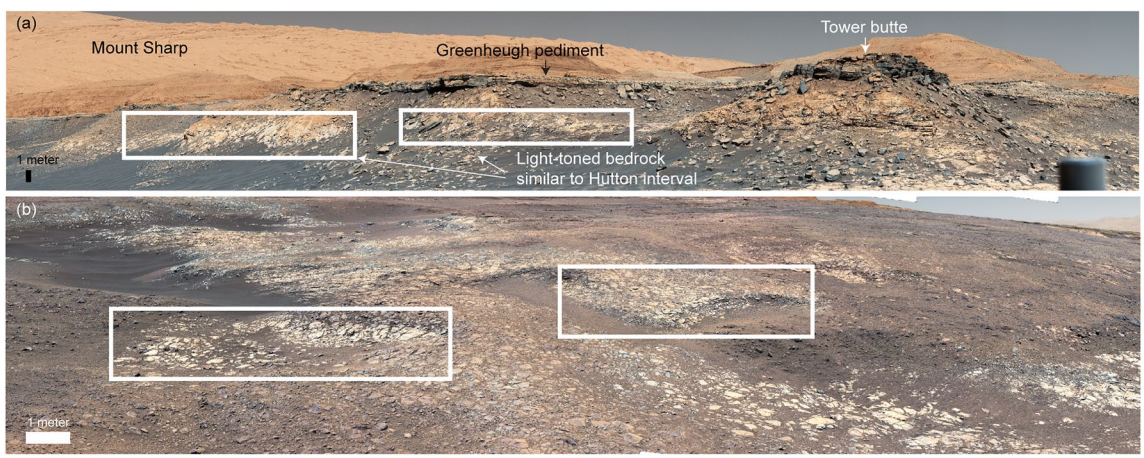

Figure 5. Light-toned bedrock zones shown in white boxes as observed by approximate natural color Mastcam mosaics. (a) Near the Hutton interval in Gm, R0 mosaic mcam13767 sol 2620, the Hutton interval is blocked in this image by Tower butte and (b) in VRR, R0 mosaic mcam10419 sol 1988.

21699100, 2022, 10, Downloaded from https://agupubs.onlinelibrary.wiley.com/doi/10.1029/2021JE007098 by Cochrane France, Wiley Online Library on [12/04/2023]. See the Terms and Conditions (https://onlinelibrary.wiley.com/terms-and-conditions) on Wiley Online Library for rules of use; OA articles are governed by the applicable Creative Commons License

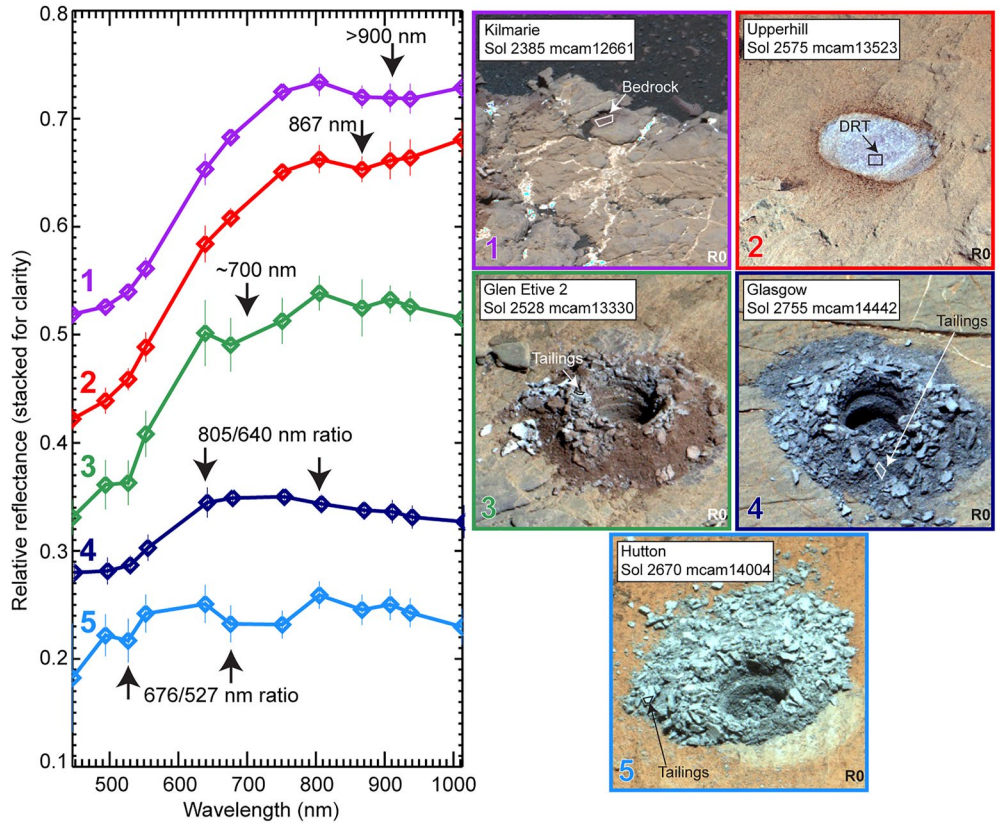

Figure 6. Type examples of Mastcam spectral features, taken from bedrock, Dust Removal Tool (DRT), and drill tailing targets. Mastcam R0 images on righthand side show Region of interest locations for spectra shown.

5. VNIR Reflectance Spectral Properties of Glen Torridon

5.1. Clay Mineral and Red Hematite Signatures

Mastcam spectra within GT show diverse spectral features including various absorption bands and spectral slopes (Figure 6). ChemCam spectra observed in drill tailings at drill sites within GT are consistent with the spectral classes defined by Mastcam multispectral data (Figure S2 in Supporting Information S1).

Many spectra exhibit a weak and broad absorption band centered >900 nm or a flat spectrum >800 nm with no clear absorptions (Figure 6, spectrum 1; Figure 7, spectra 1, 2, 5–7, and 10). Spectra of this type also exhibit a strong red slope <640 nm and a reflectance peak at 805 nm. An absorption band centered between 900 and 950 nm could be consistent with several phases, including nanophase iron oxides and Fe^{3+}-bearing smectites like nontronite. However, ferric smectites are most plausible based on their strong detections in orbital observations of GT (Fraeman et al., 2016) and CheMin models of up to 34 wt.% phyllosilicates in GT drill samples (Bristow, Grotzinger, et al., 2021; Thorpe et al., 2021, 2022). Similar spectral signatures have been observed in the SI member below VRR (Haber et al., 2020) and in isolated cm-scale patches within the VRR Jm (Horgan et al., 2020). The >900 nm band was observed in all types of ROIs (dusty bedrock, DRT spots, and drill tailings) and in all three stratigraphic members in Mastcam data, but not near the GT-Stimson contact (Figures 7 and 8). The detection of this feature is sometimes dependent on the size of the ROI selected. Large ROIs can either flatten the >900 nm absorption feature or exhibit a small band depth (~0.5%–6%), while spectra with the greatest >900 nm band depth tend to be from smaller ROIs. This issue is not as prominent with other spectral features in GT.

Spectra often exhibit a weak absorption band centered near 867 nm associated with a strong red slope <640 nm (Figure 6, spectrum 2; Figure 7, spectra 3, 4, 8, 9, and 11–16). This band position is consistent with fine-grained red crystalline hematite (Morris et al., 1989). This is consistent with CheMin analyses in GT that show minor hematite (<1 to 4 wt.%) in almost all GT drill samples (Bristow, Grotzinger, et al., 2021; Thorpe et al., 2021, 2022).

21699100, 2022, 10, Downloaded from https://agupubs.onlinelibrary.wiley.com/doi/10.1029/2021JE007098 by Cochrane France, Wiley Online Library on [12/04/2023]. See the Terms and Conditions (https://onlinelibrary.wiley.com/terms-and-conditions) on Wiley Online Library for rules of use; OA articles are governed by the applicable Creative Commons License

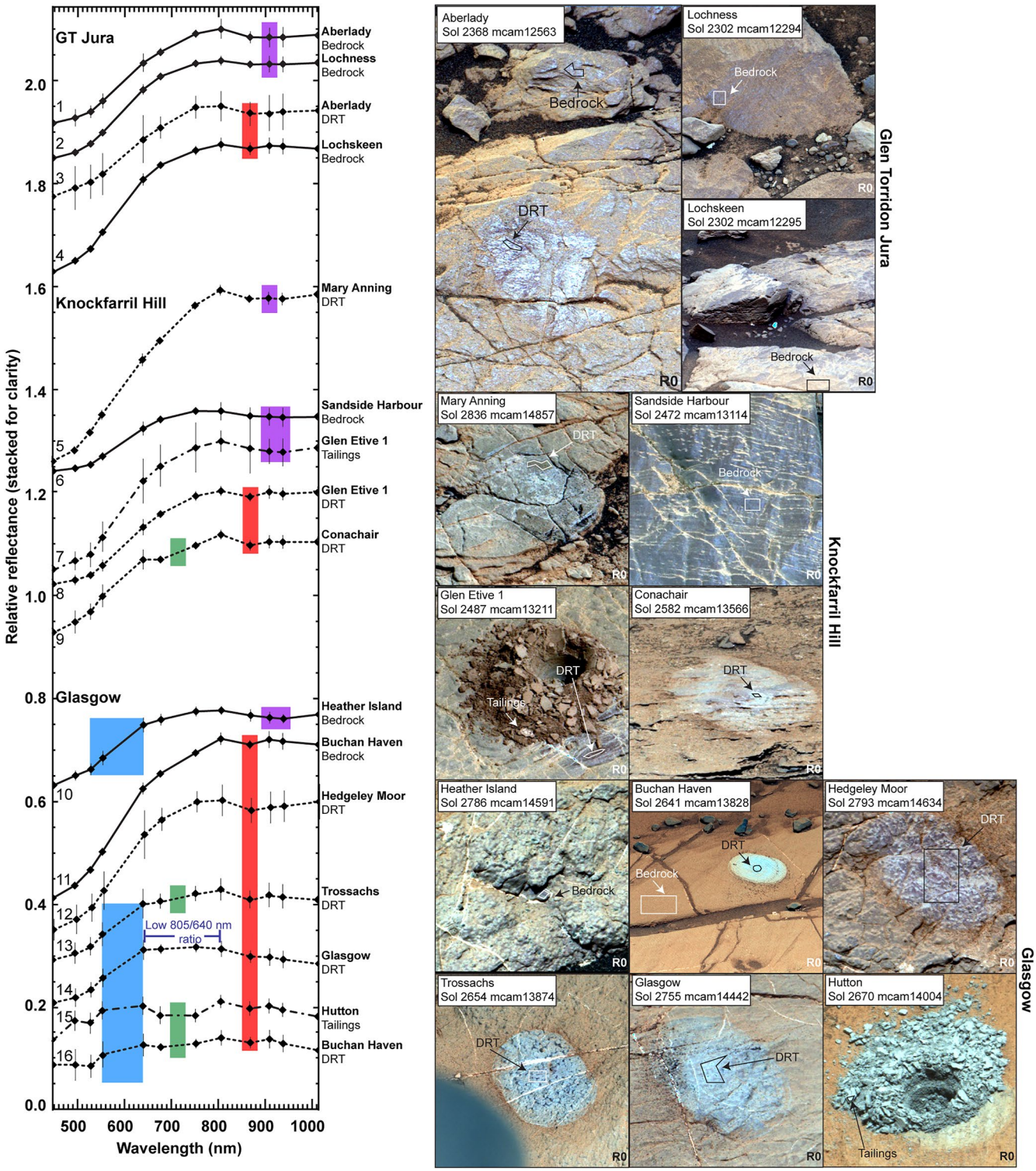

Figure 7. Mastcam spectra for all stratigraphic members of Glen Torridon (GT) (left) and corresponding enhanced color R0 images of each Region of interest (right). Solid line represents bedrock target, thin dashed line represents Dust Removal Tool (DRT) target, and dash-dot line represents tailings target. DRT spots are typically ~7.5 × 4.5 cm. Color bars on a spectrum indicate the position of key spectral features (see Figure 6).

21699100, 2022, 10, Downloaded from https://agupubs.onlinelibrary.wiley.com/doi/10.1029/2021JE007098 by Cochrane France, Wiley Online Library on [12/04/2023]. See the Terms and Conditions (https://onlinelibrary.wiley.com/terms-and-conditions) on Wiley Online Library for rules of use; OA articles are governed by the applicable Creative Commons License

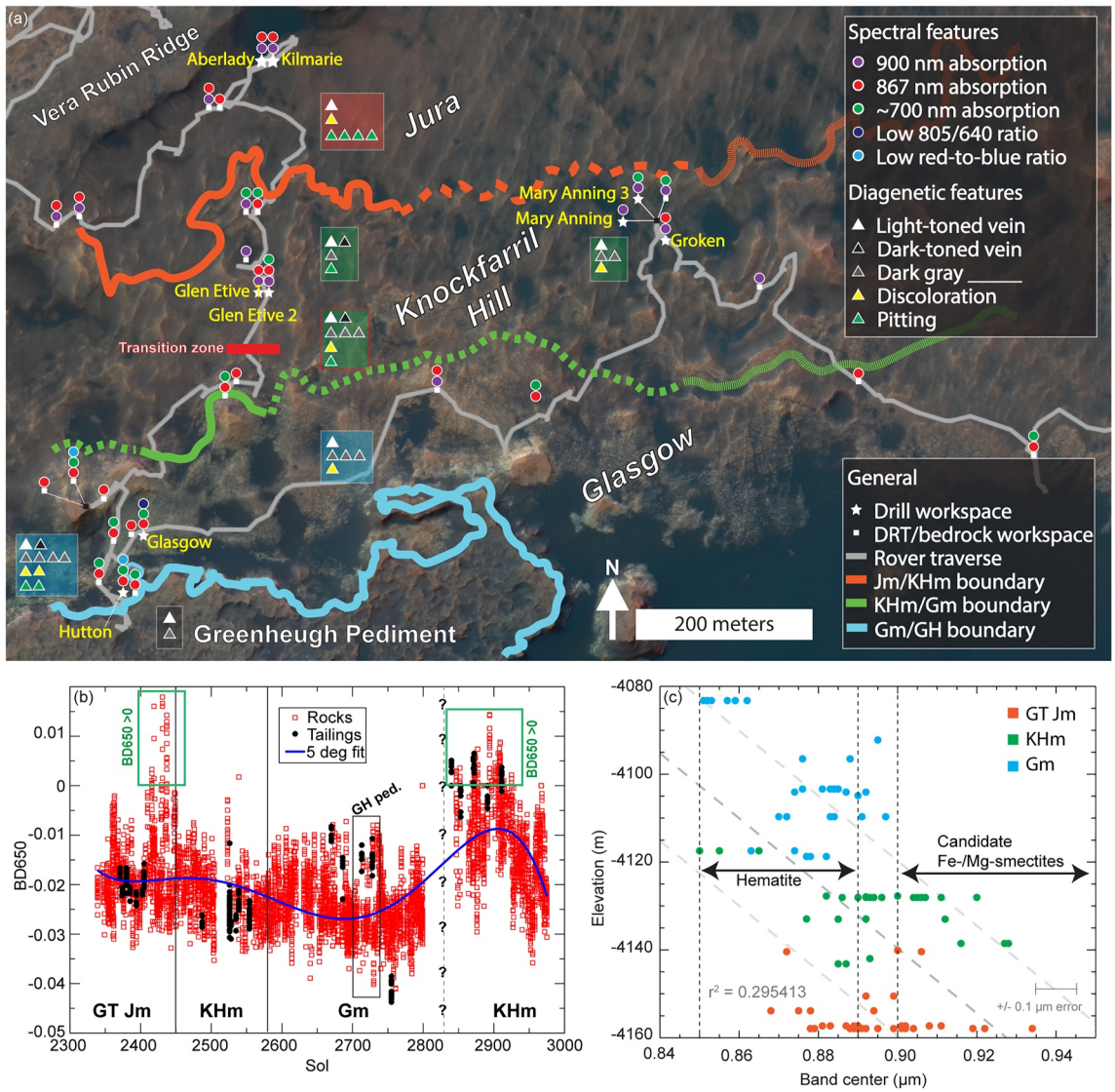

Figure 8. (a) Spectral distribution map. See map legend for spectral feature classification, workspace type (drill or DRT/bedrock), rover traverse, and stratigraphic member boundaries. Solid lines for stratigraphic member boundaries are confident boundaries; dashed lines indicate relative degree of certainty where the more frequent the dashes, the higher the boundary location. (b) Sol versus 650 nm band depth using ChemCam rock and tailings targets. Dashed line with question marks represents approximated boundary between Gm and KHm. Blue line is a 5-degree polynomial fit to the data. Green boxes indicate regions where BD650 > 0. (c) Mastcam ~900 nm band center of all targets used in this study relative to elevation in all Glen Torridon (GT) stratigraphic members. Band centers from 850 to 890 nm are consistent with hematite and band centers >900 nm are consistent with Fe-/Mg-smectites. Dashed lines indicate linear fit to data and one standard deviation.

Similar weak hematite spectral signatures are observed in Mastcam data throughout much of the Mf (Wellington et al., 2017). Spectra with an 867 nm absorption are the most widespread and are observed in all GT members (Figures 7 and 8) and all types of ROIs. Only five images on the spectral distribution map (Figure 8) do not include this absorption, all of which are in KHm. The distribution of this absorption demonstrates that red hematite is persistent throughout GT but is locally patchy.

Trends in spectral variability in VNIR spectral data are clearly highlighted when comparing long wavelength band centers observed in Mastcam with elevation (Figure 8c). In the GT Jm, band centers range from ~875 to 935 nm and ~38% of the spectra exhibit band centers >900 nm. In the KHm, band centers range from ~850 to 930 nm and ~37% of the spectra exhibit band centers >900 nm. In the Gm, band centers range from ~850 to 895 nm, and none of the spectra exhibit band centers >900 nm. Some spectra were not included due to very small band depths that could not be fit accurately. Because of this, potential weak clay mineral detections in the

21699100, 2022, 10, Downloaded from https://agupubs.onlinelibrary.wiley.com/doi/10.1029/2021JE007098 by Cochrane France, Wiley Online Library on [12/04/2023]. See the Terms and Conditions (https://onlinelibrary.wiley.com/terms-and-conditions) on Wiley Online Library for rules of use; OA articles are governed by the applicable Creative Commons License

21699100, 2022, 10, Downloaded from https://agupubs.onlinelibrary.wiley.com/doi/10.1029/2021JE007098 by Cochrane France, Wiley Online Library on [12/04/2023]. See the Terms and Conditions (https://onlinelibrary.wiley.com/terms-and-conditions) on Wiley Online Library for rules of use; OA articles are governed by the applicable Creative Commons License

Gm spectra are not shown in this plot, but they are observed in qualitative analyses at locations away from the GH pediment (Figure 8a). These band center trends support our result that smectite signatures are clearest and strongest in the GT Jm and KHm, and that hematite is present throughout all units.

All ChemCam spectra from drill tailings show a downturn to longer wavelengths (Figure S2 in Supporting Information S1; Johnson et al., 2019, 2020). The downturn into longer wavelengths could be consistent with a longer wavelength absorption, but the band center cannot be determined to differentiate between a >900 nm band and an 867 nm band (Figure 6).

Five drill tailings ChemCam spectra (Aberlady, AB; Kilmarie, KM; Glen Etive, GE; Mary Anning 1, MA1; and Groken, GR) exhibit flattening at ~650 nm (Figure S2 in Supporting Information S1). An absorption band centered ~650 nm is consistent with Fe-/Mg-smectites (i.e., nontronite) but could also be consistent with other Fe-oxides (e.g., goethite or lepidocrocite). This spectral feature is distinct from the ~700 nm absorption in Mastcam (Figure 6, spectrum 3, see Section 5.2) because it is not specifically associated with light-toned veins and tailings, but instead with tailings that are visually consistent in color with bedrock. Thus, we hypothesize that this spectral feature is due to clay minerals, and this feature is resolved in the ChemCam spectra because of the higher spectral resolution relative to Mastcam. Figure 8c shows band depth at 650 nm in all bedrock and tailings ChemCam spectra. This occurs in GT Jm, near the contact with KHm, and in KHm near MA and GR drill tailing targets, which is consistent with where we see in >900 nm band in Mastcam.

5.2. Gray Hematite Signatures

Some Mastcam spectra also exhibit a flattening or weak absorption band centered between 676 and 751 nm (~700 nm; Figure 6, spectrum 3; Figure 7, spectra 9, 13, 15, and 16). The specific band center is hard to resolve with high confidence, and thus is potentially consistent with $Fe^{2+/3+}$-phyllosilicates (including nontronite), microplaty hematite, goethite, and lepidocrocite. This spectral feature is observed in KHm and Gm (Figure 8) and is commonly associated with the 867 nm absorption (hematite), supporting an iron-oxide interpretation. This feature is most frequently observed in light-toned vein and tailings ROIs in Mastcam images. This absorption is observed with greater band depths in terrains close to the GT-Stimson contact as *Curiosity* drove away from the GH pediment. Similar spectra were observed in association with diagenetically altered gray Jm rocks on VRR, where they were also interpreted as due to iron oxides such as microplaty hematite (Horgan et al., 2020). This interpretation was supported by observations of this band in association with the few dark diagenetic features large enough to be resolved in Mastcam spectra, some of which showed iron enrichments in ChemCam LIBS measurements consistent with hematite (David et al., 2020; Horgan et al., 2020; L'Haridon et al., 2020).

A specific subset of spectra in GT exhibit enhanced reflectance at short wavelengths (low RBR) with varying intensity (Figure 6, spectra 4 and 5). Weak signatures of this type are defined by a peak shifted to shorter wavelengths, resulting in a low 805/640 nm band ratio and a weak blue slope from 640 to 1,000 nm (Figure 6, spectrum 4; Figure 7, spectra 13 and 14). These weak signatures are only observed in the DRT and tailings ROIs at the GG drill workspace and in the tailings dump pile and surrounding bedrock ROIs at the GG dump pile workspace. Strong signatures of this type are defined by a very low RBR (flat spectrum), often associated with absorptions at 527 nm, between 676 and 751 nm, and at 867 nm (Figure 6, spectrum 5; Figure 7, spectra 15 and 16). This feature is observed only in the Gm at the Buchan Haven DRT target and in the HU drill tailings. The HU drill site is located just below the GT-Stimson contact, at the Hutton interval, and Buchan Haven is on the Western Butte (Figure 8). Gm ChemCam spectra exhibit both the strong and weak low RBR features described here, with a downturn from ~640 nm observed only in GG tailings (Figure S2 in Supporting Information S1; Johnson et al., 2020).

The overall flattening of these spectra is generally consistent with a lack of Fe^{3+}-bearing minerals, including fine-grained red hematite, but could still be consistent with very spectrally flat ferric minerals (e.g., coarse-grained gray hematite or magnetite). CheMin analyses of the GG drill site show that it is not lacking in hematite, and instead has the highest wt. % of hematite in GT (~4 wt. %; Thorpe et al., 2021, 2022). CheMin analyses at HU has the lowest phyllosilicate abundance in GT at ~<10 wt. %, as well as ~6 wt. % magnetite, which is the only GT sample that has magnetite above the detection limit for CheMin (Thorpe et al., 2021, 2022). Thus, a combination of coarse gray hematite and magnetite could be responsible for the "flat" spectra in Gm. Similar "flat" spectra

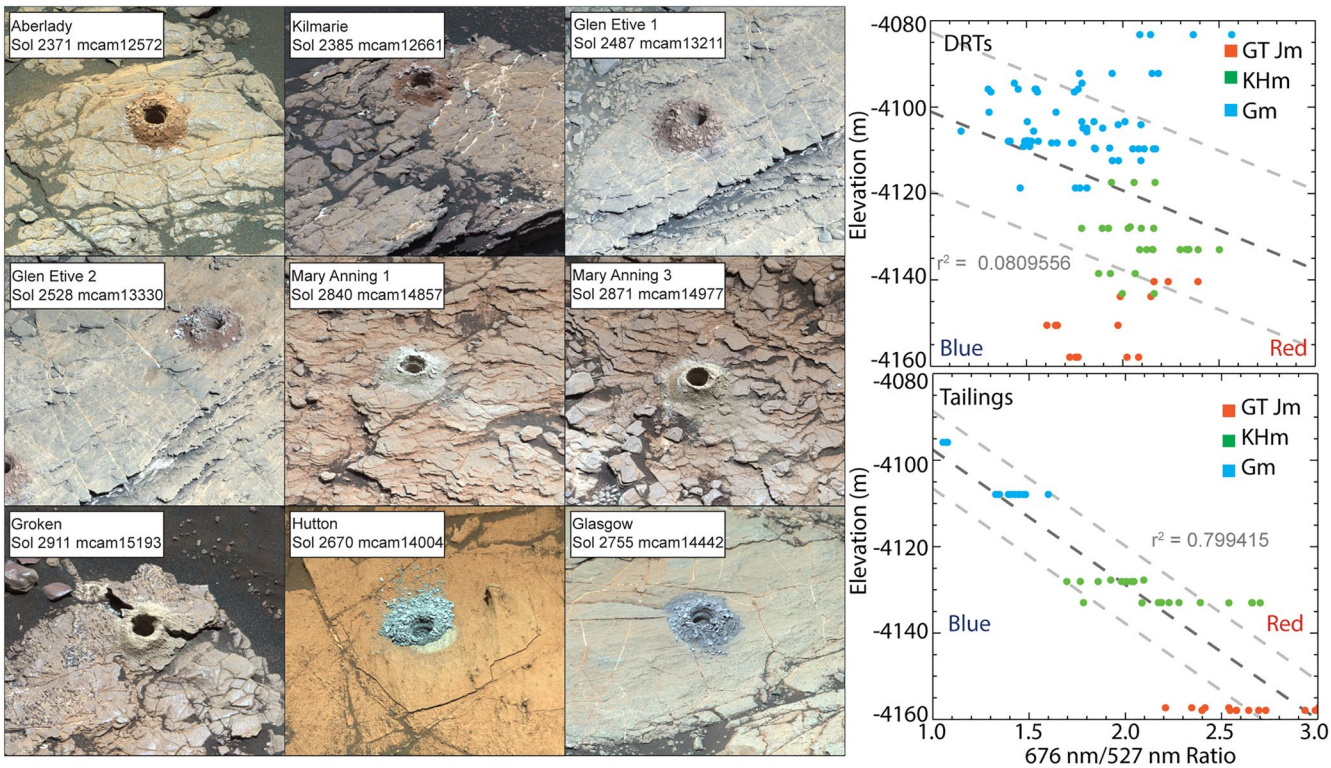

Figure 9. (Left) Approximate natural color Bayer filter (R0) images of bedrock and drill tailings at drill sites. (Right) Red-to-blue-ratio versus elevation plots for Dust Removal Tools (DRTs) (top) and drill tailing targets (bottom). Dark gray dashed line is a trend line with 1 standard deviation light gray dashed lines.

were found during the VRR campaign in association with the most altered and light-toned areas in the VRR Jm (Horgan et al., 2020).

The presence of coarse gray hematite can be tracked using the RBR of bedrock surfaces (i.e., DRTs) and drill tailings (~2–6 cm depth; Anderson et al., 2012). In general, a higher RBR is consistent with red hematite (fine) and a lower RBR is consistent with gray hematite (coarse), and previous results from VRR showed that this trend is even stronger for drill tailings. While the grain size of the tailings is apparently not high enough to cause reddening of coarse hematite upon drilling, it does seem to cause reddening of fine-grained red and nanophase hematite in bedrock, possibly due to liberation of red hematite from cements (Horgan et al., 2020).

The RBR of drill tailings clearly decreases with increasing elevation in GT from the base of GT toward the GH pediment (Figure 9), suggesting a coarsening of hematite toward the pediment in Gm. DRT targets overall show reddening on drilling in Jm, little change on drilling in KHm, and bluing on drilling in Gm, also consistent with more coarse hematite near the pediment. DRT-cleared surfaces on their own show a more complicated trend with elevation. The GT Jm has a lower RBR at lower elevations that trend to a higher RBR with elevation into KHm, where the reddest rocks are observed in the GE workspace (RBR of 2.5). Similar RBR values are observed in Gm at higher elevations to the east of and away from the GH pediment. At lower elevations in the Gm, the DRT targets experience bluing upon approaching the GH pediment (~−4,100 m), reaching the lowest RBR of all DRT targets at Buchan Haven (RBR of 1.2).

The combination of abundant dark gray diagenetic features, the increase in crystalline hematite in CheMin, and the decrease in RBR in drill tailings in Gm near the pediment suggests that targets with this "flat" spectral character may represent regions dominated by coarse-grained gray hematite. A likely origin for this material is recrystallization of fine-grained red hematite into coarse-gray hematite, as hypothesized for VRR (Horgan et al., 2020; L'Haridon et al., 2020).

21699100, 2022, 10, Downloaded from https://agupubs.onlinelibrary.wiley.com/doi/10.1029/2021JE007098 by Cochrane France, Wiley Online Library on [12/04/2023]. See the Terms and Conditions (https://onlinelibrary.wiley.com/terms-and-conditions) on Wiley Online Library for rules of use; OA articles are governed by the applicable Creative Commons License

21699100, 2022, 10, Downloaded from https://agupubs.onlinelibrary.wiley.com/doi/10.1029/2021JE007098 by Cochrane France, Wiley Online Library on [12/04/2023]. See the Terms and Conditions (https://onlinelibrary.wiley.com/terms-and-conditions) on Wiley Online Library for rules of use; OA articles are governed by the applicable Creative Commons License

6. Discussion

6.1. Mineralogy of Glen Torridon

The combination of VNIR spectral data and Mastcam images provides an outcrop-scale (meters) compositional link between large-scale (tens of meters to kilometers) orbital spectral data and highly localized (centimeters) detailed mineralogical data from the CheMin and SAM instruments. Understanding the compositional variability and distribution at this outcrop scale provides important constraints on geological interpretations of the relative timing of, and regional exposure to, early and late diagenetic events in GT.

This work demonstrates that spectral signatures consistent with Fe^{3+}-smectites modeled from CheMin data (Thorpe et al., 2021, 2022) are observable at the spectral resolution and range in Mastcam multispectral images. We observe spectral signatures consistent with some species of clay minerals throughout all stratigraphic members within GT. These spectral signatures appear to correlate to CheMin phyllosilicate abundances, as drill tailings with a higher and lower wt. % of phyllosilicates coincide with regions where spectral features consistent with clay minerals are and are not observed, respectively. Orbital analyses of Jm and KHm show signs of absorption band centers at 1.9, 2.24, and 2.8 μm which are also consistent with ferric smectites (e.g., He et al., 2019, 2022). These smectite signatures are the strongest observed from orbit in Mt. Sharp (Fox et al., 2021; Fraeman et al., 2016; Milliken et al., 2010), which we confirm based on the detection of related smectite signatures in Mastcam spectra.

In situ geochemical data from the Alpha-Particle X-ray Spectrometer (APXS) of GT Jm and KHm supports a high abundance of clay minerals in GT as well. APXS data show low K and high Mg abundances that are interpreted as related to high phyllosilicate content (O'Connell-Cooper et al., 2021, 2022). In addition, the chemical index of alteration (CIA), which is calculated using the molecular proportions: $\mathrm{CIA} = \left[\frac{Al_2O_3}{Al_2O_3 + CaO^* + Na_2O + K_2O}\right] \times 100$, and generally has a positive correlation with the presence of clay minerals (Dehouck et al., 2021, 2022; Nesbitt & Young, 1982), shows values that are higher (~50–60) throughout most of GT, and then decrease to a minimum of ~40 in Gm near the GH pediment, then returns to higher values consistent with the rest of GT in Gm farther away from the GH pediment (Dehouck et al., 2021, 2022).

The Hutton interval corresponds with the region in which fewer phyllosilicates are observed both from point data (CheMin) and in situ VNIR data (Mastcam and ChemCam). A decrease in phyllosilicate abundance from ~20 to 30 wt. % in most of GT to <10 wt. % at this location is observed (Thorpe et al., 2021, 2022), while a slight increase in hematite abundance is observed from ~<1–2 wt.% in GT Jm and KHm to ~2–4 wt. % in Gm (Thorpe et al., 2021, 2022). In this same region, no clay mineral spectral features are present in VNIR data and instead flat spectral signatures are observed that suggest a lack of fine-grained red hematite and the possible presence of coarse-grained gray hematite (Figures 6 and 7). As *Curiosity* traversed away from the pediment scarp, but still within Gm, spectral features consistent with clay minerals and fine-grained red hematite observed in earlier stratigraphic members returned. This suggests that the bulk of Gm, at one point, likely was compositionally similar to GT Jm and KHm.

We hypothesize that the Hutton interval represents a zone where clays and fine-grained red hematite were destroyed. We further hypothesize that the mechanism of this Fe-bearing mineral destruction is top-down fluid flow that occurred in a late diagenetic event in which those destroyed components were mobilized, and then some were recrystallized as coarse-grained gray hematite, possibly both locally as well as down-section (e.g., Bennett et al., 2021; David et al., 2020; L'Haridon et al., 2020). The "bleached" appearance of the Hutton interval is consistent with removal of red/purple-toned smectites and coarsening of hematite from red to gray, and many diagenetic features observed in GT and lower in the Mf indicate iron mobility during diagenesis. Dark-toned diagenetic features form due to concentrations of iron, which could be due to localized diagenesis, especially when associated with small-scale bleached halos that form due to local iron remobilization (David et al., 2020; L'Haridon et al., 2020). Alternatively, these features can also form due to larger scale iron mobility as hypothesized for VRR (Bennett et al., 2021) and in SI (Haber et al., 2020). While FeO_T wt. % is lower in Gm relative to KHm and Jm, there is a lack of geochemical evidence for large-scale iron mobility (Thompson et al., 2021, 2022), but that does not rule out localized iron mobility in GT.

21699100, 2022, 10, Downloaded from https://agupubs.onlinelibrary.wiley.com/doi/10.1029/2021JE007098 by Cochrane France, Wiley Online Library on [12/04/2023]. See the Terms and Conditions (https://onlinelibrary.wiley.com/terms-and-conditions) on Wiley Online Library for rules of use; OA articles are governed by the applicable Creative Commons License

6.2. Early Clay and Hematite Formation in Glen Torridon

The distribution of spectral features observed in GT shows that both clay minerals and fine-grained hematite are present throughout GT, except for near the GT-Stimson contact (Figure 8, blue line). Based on this ubiquitous distribution, we hypothesize that the clay minerals and fine-grained red hematite formed in the early environment. This hypothesis is further supported by the observation that regions in GT where spectral signatures of clay minerals are stronger tend to have the lowest abundance and diversity of diagenetic features, most notably the GT Jm and the KH prior to the transition zone. This suggests that the clay minerals formed early, prior to burial (see Section 6.3 for additional discussion of the timing of diagenetic features).

Clay minerals may have formed in situ in the lacustrine environment, due to pedogenesis/weathering during exposure of the sediments or may be detrital and sourced from weathering or alteration in the watershed (e.g., Worden & Morad, 1999). Their ubiquitous distribution suggests that they are authigenic rather than detrital, as the latter would more likely be correlated with depositional facies rather than across multiple units and formations, but a detrital origin cannot be ruled out. The lack of correlation between clay mineral abundance and grain size, as observed from similar wt. % of phyllosilicate detection (Thorpe et al., 2021, 2022) and continuity of spectral features in GT Jm to KHm, while the latter has a higher percentage of coarser grains (Rivera-Hernández, Sumner, Minitti, et al., 2020), further supports an authigenic origin of clay minerals. Finally, chemical data from GT also supports clay formation through early weathering and limited later alteration in clay-rich regions. APXS shows that lithologies that are the most phyllosilicate-rich appear to be the least geochemically altered, partially based on the GT Jm having very low $CaSO_4$ which is associated with alteration and diagenesis (O'Connell-Cooper et al., 2021, 2022).

Similar but stronger clay-like spectral signatures are observed in Mastcam data from SI (Figure 1; Haber et al., 2020). This is consistent with APXS data that show that GT Jm and SI have the greatest geochemical overlap when compared to other lower stratigraphic members in Gale crater (O'Connell-Cooper et al., 2021, 2022). These signatures in SI are associated with evidence for sub-aerial exposure in the form of desiccation cracks and sulfate enrichment (Rapin et al., 2019), and the smectites observed are hypothesized to be the result of surface weathering (Haber et al., 2020; Stein et al., 2018). The lack of this type of physical evidence for surface exposure in GT could either suggest that exposure and weathering was more limited than in SI, or that the GT clays formed through other authigenic formation mechanisms, such as alteration in the lake environment.

Fine-grained red hematite is also ubiquitous throughout GT but is most apparent outside of the bleached zones, suggesting that it also formed early. Fine-grained hematite may have formed due to oxidation within the lake itself (Hurowitz et al., 2017), due to early interactions with oxidizing groundwater (Rampe et al., 2017; Rampe, Bristow, et al., 2020), or due to oxidation during early exposure/weathering (Worden & Morad, 1999). There appears to be a local anti-correlation between hematite and clay minerals, in both multispectral and CheMin data, where more clay minerals are observed, less hematite is observed (Thorpe et al., 2021, 2022). Whether this is an early environment indicator (e.g., local variability in exposure) or a change related to later diagenesis is not clear.

6.3. Timing of Diagenesis in Glen Torridon

Diagenetic features can be used to constrain the timing and chemistry of diagenetic fluid activity, although this can be challenging as many diagenetic processes can occur at any point during emplacement, burial, or exhumation of rocks. Diagenetic features in GT that we attribute to early diagenesis include crystal molds and features that we attribute to late diagenesis include fracturing and veins. Crystal molds and features likely precipitated during early diagenesis based on a lack of disruption or deformation to primary sedimentary features where observed (e.g., laminations; Bennett et al., 2021). Fracturing occurs due to the compaction and relief of pressure during the lithification process (compaction and exhumation) and thus fracture mineral fills (i.e., veins) are attributed to fluid flow through these fractures during late diagenesis (e.g., Bennett et al., 2021; Kronyak et al., 2019). More ambiguously timed diagenetic features include dark gray diagenetic features, casings, nodules, and overall discoloration. Ambiguously timed features have not been constrained to forming at the surface or at depth but are indicative of mobility of elements via diagenetic fluid flow (e.g., Bennett et al., 2021; Sun et al., 2019)

GT Jm and KHm both exhibit low overall density and diversity of diagenetic features, and the diagenetic features that are present are consistent with early diagenesis (star-shaped and rectangular pits). These early diagenetic features also occur on VRR and are concentrated in VRR Jm (Bennett et al., 2021). The lack of pervasive late

21699100, 2022, 10, Downloaded from https://agupubs.onlinelibrary.wiley.com/doi/10.1029/2021JE007098 by Cochrane France, Wiley Online Library on [12/04/2023]. See the Terms and Conditions (https://onlinelibrary.wiley.com/terms-and-conditions) on Wiley Online Library for rules of use; OA articles are governed by the applicable Creative Commons License

diagenetic features throughout the GT Jm and lower portion of the KHm suggest that at least the bottom-most members of GT did not experience, or were not heavily altered by, later diagenetic events. This implies that the current composition of bedrock in those stratigraphic members is most representative of the early surface environment and can be used to constrain deposition and alteration processes prior to lithification. In GT this includes sedimentation in a lake environment and possible formation of clay minerals through pedogenesis. This is consistent with our interpretation above that the clay minerals and hematite found in these members formed through early weathering or lacustrine processes. This interpretation is also consistent with the geochemistry of GT Jm and KHm that do not show trends or heterogeneity that would be expected for late diagenetic alteration (O'Connell-Cooper et al., 2021, 2022).

The upper portion of the KHm is distinct, and we hypothesize that the "transition-zone" within the KHm is a diagenetic front. While this transition zone is not clearly defined from the spectral perspective, Mastcam and MAHLI images throughout KHm show an increase in abundance and type of diagenetic features after sol 2563 prior to *Curiosity* encountering the buttes but near where bedrock appears to be more fractured from orbit (Figure 1). Because this transition does not correspond to stratigraphic member boundaries, we attribute it to later diagenesis rather than variability in the depositional environment. In KHm after sol 2800, there is still an increase abundance and diversity of diagenetic features thus not restricting later diagenesis in KHm to being dependent on interactions related to the modern GH pediment. We hypothesize that the diagenetic event that formed the "transition-zone" may have been a separate event, prior to the diagenetic event that caused the alteration proposed around the Hutton interval.

The Gm exhibits the most pervasive signs of late diagenesis both spectrally and morphologically relative to the lower stratigraphic members in GT. The strongest signatures that we attribute to late diagenesis (e.g., flattening of spectra, lack of absorptions consistent with clay minerals, color-change in bedrock, high abundance and diversity of diagenetic features) are all observed close to the contact between Gm and the GH pediment capping unit (sols 2581–2801, Table 1). Within Gm but away from the GH pediment (sols 2951–2975), this stratigraphic member has diagenetic and spectral features that are comparable to the upper, more altered regions of KHm (sols 2564–2580, 2901–2950). This is consistent with an increase in degree of alteration toward the pediment, and we hypothesize that this could be due to at least one additional diagenetic episode in the region of the GT-Stimson contact.

The Stimson near GT (i.e., GH pediment capping unit) does not appear to be highly altered based on the relatively high abundance of primary minerals (>30 wt. % plagioclase, >20 wt. % pyroxene, and >8 wt. % olivine; Bedford et al., 2021, 2022; Thorpe et al., 2021, 2022). But signs of alteration in the form of diagenetic features are observed at its contact with the Gm (Table 1) and phyllosilicates were detected in the Stimson by CheMin (e.g., Thorpe et al., 2021, 2022). This suggests that diagenetic fluids may have flowed through the more permeable Stimson formation to interact with the underlying Gm and that at least some of the diagenetic events occurred after its deposition in this region, but likely not all.

6.4. Controls on Diagenesis in and Around Glen Torridon

Understanding the relationship between GT and VRR is critical for reconstructing the diagenetic history of the region. CheMin analyses show a high hematite abundance (up to ∼15 wt. %) and a low phyllosilicates abundance (up to ∼15 wt. %) on VRR relative to GT (Rampe, Bristow, et al., 2020). In Mastcam data, there is a notable lack of >900 nm smectite-like spectral signatures in VRR, with only a few possible detections in the VRR Jm (Horgan et al., 2020), likely due to the high abundance of hematite (Rampe, Bristow, et al., 2020). GT and VRR share similar spectral signatures consistent with Fe-oxides, including fine-grained red hematite throughout both regions and patchy signatures attributed to coarse-grained gray hematite. They also exhibit similar diagenetic features, as all the diagenetic features observed throughout GT are also seen in VRR, apart from casings (Bennett et al., 2021). Most notably, both regions contain light-toned bedrock with coarse-grained gray hematite that are attributed to bleaching through hematite recrystallization, suggesting that both regions experienced extensive late diagenesis (Horgan et al., 2020).

While broad similarities exist between GT and VRR, there are very few similarities within the stratigraphic member that they share (Jm). This division is likely due to late diagenesis preferentially cementing the VRR Jm (Fraeman et al., 2020) as there is very little evidence of late diagenetic alteration in GT Jm. This is supported by

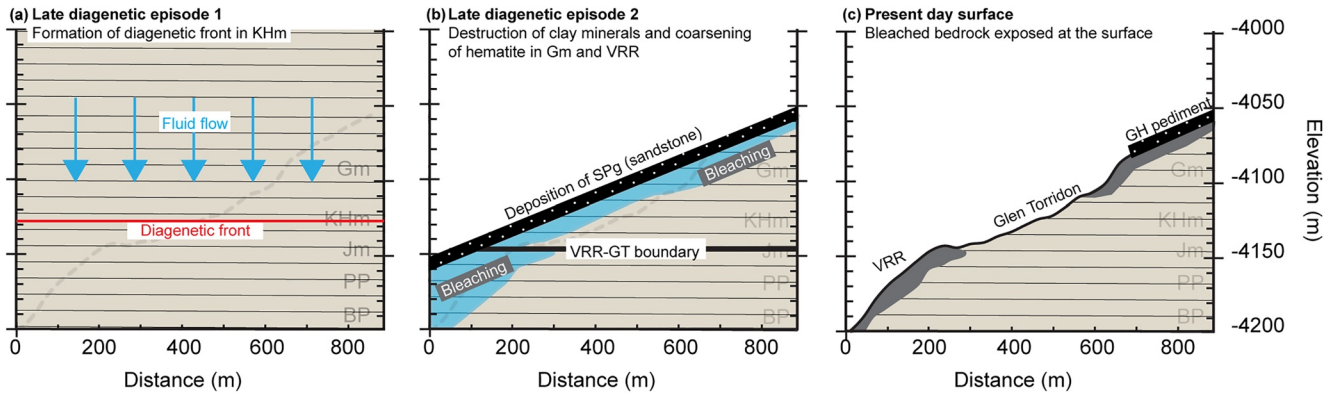

Figure 10. Conceptual cross-section model to explain different potential late diagenetic events that occurred in Glen Torridon (GT) and surrounding areas. (a) Corresponds with model step 4 that formed the diagenetic front in Knockfarril Hill (KHm), (b) corresponds with model steps six and seven in which the Siccar Point group sandstones are deposited and lithified and later diagenesis that led to the coarsening of hematite and destruction of clay minerals, and (c) corresponds with the present-day surface, with exposed bleached bedrock in Vera Rubin ridge (VRR) and upper GT.

geochemical analyses that show that GT Jm and VRR Jm exhibit distinct bulk chemistries (O'Connell-Cooper et al., 2021, 2022). We hypothesize that a similar high abundance of clay minerals was present in the early environment in the VRR Jm as in GT Jm but that most of these clay minerals were destroyed or altered to phases not detectable by Mastcam (e.g., Fe-poor phyllosilicates and/or amorphous materials) during diagenesis (Bristow, Grotzinger, et al., 2021; Rampe, Bristow, et al., 2020). This and any later diagenetic fronts did not penetrate the portions of Jm currently exposed in GT, and so diagenetic activity may have only altered the Jm where it is preserved on VRR.

We hypothesize that the presence of clay minerals, the grain size of sediments, and the porosity of sediments affected the flow of later diagenetic fluids in and around GT and thus affected where greater degrees of diagenetic alteration occurred. In this model, limited diagenesis in clay mineral-rich rocks of GT and extensive diagenesis in the VRR (Horgan et al., 2020) and Gm is due to early clay mineral deposits affecting the flow of diagenetic fluids. The impermeable clay minerals in Jm and KHm would have prevented significant through-going fluid flow and would have instead focused diagenetic fluids and alteration to the margins of these clay mineral-rich units. When diagenetic fluids encountered the clay region, the fluids would have moved slowly and/or become trapped, leading to enhanced alteration on the edges of this region (i.e., enhanced alteration in VRR Jm and Gm; Figure 10). The patchiness of diagenetically altered gray zones in VRR Jm is consistent with heterogeneous diagenesis observed in impermeable clay-rich mudstones on Earth due to restricted fluid flow in these types of rocks (e.g., Gutzmer & Beukes, 1998; Tardy, 1992; Worden & Morad, 1999).

Additionally, the high porosity and permeability of the sandstones in the GH pediment capping unit could have caused it to act as a conduit for fluid flow. Any fluid that flowed to the base of the sandstone unit would have encountered the relatively impermeable underlying mudstones, which would have acted as a barrier to fluid flow, leading to significant alteration in Gm at the GT-Stimson contact. The Stimson may have at one point extended farther downslope and overlain the VRR (Fraeman et al., 2016), leading to the similarities that we see in Gm and VRR. At greater depths from this contact, geologic units are less altered and preserve more textures and minerals related to deposition and early diagenesis.

6.5. Proposed Geologic Timeline in Glen Torridon

Deciphering the history of diagenetic events is challenging on Mars, but the available evidence described above suggests the following proposed sequence of events (Figure 10). This proposed and simplified model encompasses the regions from SI through to the GH pediment capping unit. For this model, we assume a perennial lake environment. This model is informed by previously proposed models (e.g., Fraeman et al., 2020; Hurowitz et al., 2017; Rampe et al., 2017; Thorpe et al., 2021, 2022), with additions focusing on the distribution of diagenetic features and alteration products observed in this work. The order outlined here does not represent a purely

21699100, 2022, 10, Downloaded from https://agupubs.onlinelibrary.wiley.com/doi/10.1029/2021JE007098 by Cochrane France, Wiley Online Library on [12/04/2023]. See the Terms and Conditions (https://onlinelibrary.wiley.com/terms-and-conditions) on Wiley Online Library for rules of use; OA articles are governed by the applicable Creative Commons License

21699100, 2022, 10, Downloaded from https://agupubs.onlinelibrary.wiley.com/doi/10.1029/2021JE007098 by Cochrane France, Wiley Online Library on [12/04/2023]. See the Terms and Conditions (https://onlinelibrary.wiley.com/terms-and-conditions) on Wiley Online Library for rules of use; OA articles are governed by the applicable Creative Commons License

linear timeline, as multiple processes can occur at the same time and a single process described can occur multiple times.

1. *Deposition of Murray and Carolyn Shoemaker formations' sediments*. The original Mf and CSf sediments were deposited in a fluviolacustrine environment as flat lying mudstones and sandstones (Fedo et al., 2020, 2022).
2. *Early diagenesis (formation of clays and Fe-oxides).* Where sediments are subaerially exposed or in stagnant shallow water, surface weathering could have formed dioctahedral clays. This process often occurs in terrestrial lake environments (e.g., Bristow, Derkowski, et al., 2021). Additionally, where sediments are submerged in shallow moving or evaporating waters, oxidation occurs to form fine-grained red hematite (e.g., Fraeman et al., 2020; Hurowitz et al., 2017; Rampe et al., 2017). Diagenetic features that might have formed in this period are crystal molds and features.
3. *Burial and lithification of Glen Torridon sediments*. Steps 1 and 2 continue over time during the construction of Mt. Sharp, burying and lithifying the sediments into the sedimentary layers. The sulfate unit was also deposited, but whether it was deposited prior to or after lithification of the lower stratigraphic units is unclear. Further study is required to constrain the effects of this unit, but it likely influenced any later diagenesis (e.g., Bristow, Grotzinger, et al., 2021).
4. *Late diagenesis of Glen Torridon at depth*. There is evidence for at least two separate late diagenetic episodes, one described here and the other in step 7 (Figure 10). The water source for these diagenetic fluids is presently unknown, but could be from groundwater, meteoric water, or some combination of these, and may have changed with each diagenetic episode. The timing of late diagenesis is not well constrained, but the presence of filled fractures suggests that at least some diagenesis post-dated burial and lithification. In this episode, diagenetic fluids flowed into Gm and KHm but were prevented from penetrating beyond the transition zone in KHm by the impermeability of the clay-bearing KHm and Jm. Diagenetic features observed in KHm that may be due to this event include dark-toned veins, dark gray features, bedrock discoloration, and large-scale pitting.
5. *Erosion and exhumation of Murray and Carolyn Shoemaker formations*. Aeolian abrasion eroded the surface to form the topography that resembles modern day Mt. Sharp (Malin & Edgett, 2000). Surface weathering may have occurred at this time, but there is no clear evidence of this type of diagenesis preserved. Fractures formed during erosion or exhumation of lithified sediments (e.g., Kronyak et al., 2019).
6. *Deposition and lithification of Siccar Point group*. During a drier period in Gale crater, the aeolian basaltic sediments of the SPg were deposited, overlying the lithified Mf (Fraeman et al., 2016). This contact is unconformable. These sediments must also have been buried and lithified to form the sandstone we see today.
7. *Late diagenesis in relation to the Greenheugh Pediment capping unit*. This diagenetic event likely occurred after step 4 and our preferred hypothesis is that it also occurred after the deposition and lithification of SPg, but prior to the erosion to the modern surface. In this scenario we hypothesize that the GH pediment capping unit extended down to the VRR. Diagenetic fluids were focused down the sandstone SPg unit and upon encountering the impermeable clay-rich units of Jm, KHm, and Gm were trapped as an aquitard at their uppermost boundaries (Gm in GT and Jm in VRR). Stratigraphic members with a contact with the SPg experienced greater alteration. However, we cannot rule out that this diagenetic event could have occurred prior to the deposition of SPg, when the unconformity at the base of the pediment was exposed as a paleosurface. Overall, diagenetic features increase in both diversity and abundance in Gm, which supports this additional diagenetic event. Features unique to Gm that suggest multiple exposures to diagenetic fluids include hollow circular features and casings that require dissolution of previously formed diagenetic features (Figure 4g).
8. *Erosion and exhumation to the modern surface*. Erosion removes the majority of the SPg and exposes the underlying Mf and CSf. Diagenetically cemented VRR resists erosion and forms a ridge while less cemented GT erodes to form a valley.

6.6. Implications

Our results demonstrate that the sediments in Glen Torridon on Mt. Sharp in Gale crater experienced a complex and extended aqueous history that included surface water and subsurface water. While the specific timing of the deposition and alteration of sediments in GT are not known, the Mf as a whole was likely deposited prior to ~3.3 to 3.2 Ga based on crater retention ages of overlying units (Grant et al., 2014), and jarosite at lower elevations in the Mf has been dated with K-Ar dating to be as young as 2.12 ± 0.36 Gyr, suggesting very late diagenesis (Martin et al., 2017). This suggests that diagenesis in Gale, and possibly on Mars, extended into the Amazonian era, over a billion years after lacustrine deposition in the original environment.

21699100, 2022, 10, Downloaded from https://agupubs.onlinelibrary.wiley.com/doi/10.1029/2021JE007098 by Cochrane France, Wiley Online Library on [12/04/2023]. See the Terms and Conditions (https://onlinelibrary.wiley.com/terms-and-conditions) on Wiley Online Library for rules of use; OA articles are governed by the applicable Creative Commons License

The relationships we report here between clay minerals and diagenesis provide compelling information regarding the preservation of biosignatures on Mars. It is known that clay minerals are abundant on the surface of Mars (e.g., Ehlmann et al., 2011) and have a unique structure that allows for the preservation of biosignatures (e.g., Summons et al., 2011; Velde, 1995; Wattel-Koekkoek et al., 2003). We now know that large clay mineral deposits in sedimentary basins on Mars can preserve some semblance of the primary environment in which they formed and that they can significantly decrease the flow of diagenetic fluids, further increasing the chance of preserving biosignatures. In addition, many areas that have experienced extensive late diagenetic alteration show patchy variations in albedo that cross stratigraphy and can be identified from orbit. Now that we know what early and late diagenesis looks like from the ground and orbit, this can be applied to other places on Mars to search for other well-preserved potentially habitable ancient environments.

Additionally, the identification of spectral features using multispectral data in this work can be used to help select future drill sites for MSL and similar techniques could be used to inform sample selection sites on Mars 2020 with the Mastcam-Z instrument (Bell et al., 2021). Sites where a > 900 nm absorption is observed may have a high abundance of Fe-bearing clay minerals, which have a high biosignature preservation potential that warrants further investigation at that region. Whereas sites with low RBR and negative slopes into long wavelengths may be regions that have experienced enhanced diagenetic alteration and thus any biosignatures are more likely to have been destroyed.

7. Conclusion

In this study, we have combined landscape-scale mineralogy from spectral observations with small-scale morphology from high resolution imaging to better understand the history of early alteration and late diagenetic processes in GT. The bedrock in this area shows clear physical and spectral evidence for both early and late diagenesis, although the exact number and timing of diagenetic events is challenging to precisely determine. Evidence of early diagenesis is in the form of crystal molds (i.e., star-shaped and rectangular pits) as well as the widespread clay minerals and fine-grained red hematite that likely formed during early surface weathering or in the early lake environment. Evidence of late diagenesis is observed near the GT-Stimson contact, in the form of bedrock bleaching, pervasive diagenetic features indicating multiple episodes of diagenesis, and the likely cannibalization of clay minerals, hence the decrease in their detections both through VNIR spectra and CheMin quantitative mineralogy (Thorpe et al., 2021, 2022).

Clay minerals in GT likely formed in the early surface environment in Gale crater. Spectral observations show that clay minerals are uniformly distributed throughout GT Jm and KHm, and that they occur along with small amounts of red, fine-grained hematite with locally variable abundance, crystallinity, and/or grain size. The ubiquity of clay minerals and fine-grained red hematite in Jm and KHm, along with the low density and diversity of diagenetic features in those units, suggests that they formed prior to lithification. The clay minerals may have formed either through alteration in a lacustrine environment or laterally extensive surface weathering, whether the altered sediments were detrital or authigenic. Similar patchy clay and hematite spectral signatures in SI below VRR have been attributed to similar weathering and diagenetic processes (Haber et al., 2020). In contrast, the lack of clay spectral signatures on VRR may be due to destruction of clay minerals by late diagenetic alteration (e.g., Bristow, Grotzinger, et al., 2021; Horgan et al., 2020; Rampe, Bristow, et al., 2020).

Our results show that diagenetic histories can vary significantly even within small areas on Mars due to variations in the mineralogy and grain size of the bedrock, and that this has significant implications for the search for life on Mars. Areas with strong Mastcam and CRISM (Compact Reconnaissance Imaging Spectrometer for Mars; Murchie et al., 2007) clay mineral spectral signatures in GT exhibit few diagenetic features, suggesting that regions where clay minerals are present represent less diagenetically altered bedrock. In addition to the unique structure of clay minerals that allow for the preservation of biosignatures at small scales (e.g., Summons et al., 2011; Velde, 1995; Wattel-Koekkoek et al., 2003), they also appear to restrict the flow of diagenetic fluids that may have otherwise destroyed any biosignatures. This suggests that in Gale crater, the clay mineral-rich region of GT best preserves both the early environment when water was present on the surface and is the most likely place to have preserved any signs of ancient life from that surface environment. Organic analyses from the SAM instrument suite support this claim, as the highest diversity and abundance of organic molecules ever detected on Mars is observed in GT (Millan et al., 2021). Clay minerals are common in ancient terrains on Mars,

21699100, 2022, 10, Downloaded from https://agupubs.onlinelibrary.wiley.com/doi/10.1029/2021JE007098 by Cochrane France, Wiley Online Library on [12/04/2023]. See the Terms and Conditions (https://onlinelibrary.wiley.com/terms-and-conditions) on Wiley Online Library for rules of use; OA articles are governed by the applicable Creative Commons License

and our results suggest that clay-rich bedrock could act as an aquitard and prevent diagenesis, further supporting the interest in the searching for biosignatures in clay-rich terrains on Mars.

Data Availability Statement

All Mastcam and Mars Hand Lens Imager images used in this manuscript are on the Planetary Data System (PDS) Geosciences Node (Edgett, 2013; Malin, 2013), as well as the HiRISE data used in this manuscript (McEwen, 2007). All ChemCam spectra used in this manuscript are available through the PDS Geosciences node (Johnson & Ward, 2022). Derived Mastcam and ChemCam data used in this paper are available (Rudolph & Johnson, 2022).

Acknowledgments
We thank the MSL mission team for their hard (virtual) work whilst facing all the challenges that have come with the COVID-19 global pandemic and collecting the data that enabled this work. We also thank the U.S. Geological Survey Astrogeology Science Center and anonymous reviewers for helpful comments and discussion, and Michael St. Clair and Million Concepts, LLC for Mastcam supplemental data information. This material is based upon work supported by the National Science Foundation Graduate Research Fellowship Program under Grant No. DGE-1842166.

References

Achilles, C. N., Rampe, E. B., Gabriel, T. S. J., Ming, D. W., Morris, R. V., Sutter, B., et al. (2020). Factors influencing the formation and abundance of X-ray amorphous materials detected in Gale Crater mudstones and sandstones. In *51st Lunar and Planetary Science Conference*.

Adams, J. B. (1968). Lunar and Martian surfaces: Petrologic significance of absorption bands in the near-infrared. *Science*, *159*(3822), 1453–1455. https://doi.org/10.1126/science.159.3822.1453

Anderson, R. C., Jandura, L., Okon, A. B., Sunshine, D., Roumeliotis, C., Beegle, L. W., et al. (2012). Collecting samples in Gale Crater, Mars; an overview of the Mars Science Laboratory sample acquisition, sample processing and handling system. *Space Science Reviews*, *170*(1–4), 57–75. https://doi.org/10.1007/s11214-012-9898-9

Anderson, W. L., & Stucki, J. W. (1979). Effect of structural Fe2+ on visible absorption spectra of nontronite suspensions. *Developments in Sedimentology*, *27*, 75–83. https://doi.org/10.1016/s0070-4571(08)70703-9

Arvidson, R. E., Squyres, S. W., Bell, J. F., Catalano, J. G., Clark, B. C., Crumpler, L. S., et al. (2014). Ancient aqueous environments at Endeavour Crater, Mars. *Science*, *343*(6169), 1248097. https://doi.org/10.1126/science.1248097

Banham, S. G., Gupta, S., Bryk, A. B., Rubin, D. M., Edgett, K. S., Dietrich, W. E., et al. (2020). Reconstruction of Aeolian palaeoenvironments and past climate events at this Greenheugh pediment, Aeolis Mons, Mars. In *52nd Lunar and Planetary Science Conference*.

Banham, S. G., Gupta, S., Rubin, D. M., Bedford, C. C., Edgar, L., Bryk, A., et al. (2022). Evidence for fluctuating wind in shaping an ancient Martian dune field: The Stimson formation at the Greenheugh pediment, Gale crater. *Journal of Geophysical Research: Planets*, *127*, e2021JE007023. https://doi.org/10.1029/2021JE007023

Banham, S. G., Gupta, S., Rubin, D. M., Watkins, J. A., Sumner, D. Y., Edgett, K. S., et al. (2018). Ancient Martian Aeolian processes and palaeomorphology reconstructed from the Stimson formation on the lower slope of Aeolis Mons, Gale Crater, Mars. *Sedimentology*, *65*(4), 993–1042. https://doi.org/10.1111/sed.12469

Bedford, C. C., Banham, S., Bowden, D., Bridges, J. C., Smith, R., Forni, O., et al. (2021). Identifying Ancient dune processes in the Stimson formation of Gale crater using geochemical data from ChemCam – New insights from the Greenheugh capping unit. *52nd Lunar and Planetary Science Conference*, *2021*, 1569.

Bedford, C. C., Banham, S., Bridges, J. C., Forni, O., Cousin, A., Bowden, D., et al. (2022). An insight into ancient Aeolian processes and post-Noachian aqueous alteration in Gale Crater, Mars, using ChemCam geochemical data from the Greenheugh capping unit. *Journal of Geophysical Research: Planet*, *127*, e2021JE007100. https://doi.org/10.1029/2021je007100

Bedford, C. C., Schwenzer, S. P., Bridges, J. C., Banham, S., Wiens, R. C., Gasnault, O., et al. (2020). Geochemical variation in the Stimson formation of Gale crater: Provenance, mineral sorting, and a comparison with modern Martian dunes. *Icarus*, *341*, 113622. https://doi.org/10.1016/j.icarus.2020.113622

Bell, J. F., Godber, A., McNair, S., Caplinger, M. A., Maki, J. N., Lemmon, M. T., et al. (2017). The Mars Science Laboratory curiosity rover Mastcam instruments: Preflight and in-flight calibration, validation, and data archiving. *Earth and Space Science*, *4*(7), 396–452. https://doi.org/10.1002/2016ea000219

Bell, J. F., Maki, J. N., Mehall, G. L., Ravine, M. A., Caplinger, M. A., Bailey, Z. J., et al. (2021). The Mars 2020 perseverance rover mast Camera zoom (Mastcam-Z) multispectral, stereoscopic imaging investigation. *Space Science Reviews*, *217*(1), 24. https://doi.org/10.1007/s11214-020-00755-x

Bennett, K., Fox, V., Bryk, A. B., Dietrich, W., Fedo, C., Dehouck, E., et al. (2022). The Curiosity Rover's Exploration of Glen Torridon, Gale crater, Mars: An Overview of the Campaign and Scientific Results. *Journal of Geophysical Research: Planets*, *127*, e2022JE007185. https://doi.org/10.1029/2022JE007185

Bennett, K. A., Rivera-Hernández, F., Tinker, C., Horgan, B., Fey, D. M., Edwards, C., et al. (2021). Diagenesis revealed by fine-scale features at Vera Rubin Ridge, Gale Crater, Mars. *Journal of Geophysical Research: Planets*, *126*(5). https://doi.org/10.1029/2019je006311

Bibring, J. P., Langevin, Y., Mustard, J. F., Poulet, F., Arvidson, R., Gendrin, A., et al. (2006). Global mineralogical and aqueous Mars history derived from OMEGA/Mars express data. *Science*, *312*(5772), 400–404. https://doi.org/10.1126/science.1122659

Bishop, J. L., Fairén, A. G., Michalski, J. R., Gago-Duport, L., Baker, L. L., Velbel, M. A., et al. (2018). Surface clay formation during short-term warmer and wetter conditions on a largely cold ancient Mars. *Nature Astronomy*, *2*(3), 206–213. https://doi.org/10.1038/s41550-017-0377-9

Bishop, J. L., Lane, M. D., Dyar, M. D., & Brown, A. J. (2008). Reflectance and emission spectroscopy study of four groups of phyllosilicates: Smectites, kaolinite-serpentines, chlorites, and micas. *Clay Minerals*, *43*(1), 35–54. https://doi.org/10.1180/claymin.2008.043.1.03

Bristow, T. F., Bish, D. L., Vaniman, D. T., Morris, R. V., Blake, D. F., Grotzinger, J. P., et al. (2015). The origin and implications of clay minerals from Yellowknife Bay, Gale Crater, Mars. *American Mineralogist*, *100*(4), 824–836. https://doi.org/10.2138/am-2015-5077ccbyncnd

Bristow, T. F., Derkowski, A., Blake, D., Berlanga, G., & Deckker, P. D. (2021). A comparative study of clay mineral authigenesis in terrestrial and Martian Lakes; an Australian example.pdf. *American Journal of Science*, *321*(7), 1080–1110. https://doi.org/10.2475/07.2021.03

Bristow, T. F., Grotzinger, J. P., Rampe, E. B., Cuadros, J., Chipera, S. J., Downs, G. W., et al. (2021). Brine-driven destruction of clay minerals in Gale Crater, Mars. *Science*, *373*(6551), 198–204. https://doi.org/10.1126/science.abg5449

Bristow, T. F., Rampe, E. B., Achilles, C. N., Blake, D. F., Chipera, S. J., Craig, P., et al. (2018). Clay mineral diversity and abundance in sedimentary rocks of Gale Crater, Mars. *Science Advances*, *4*(6). eaar3330. https://doi.org/10.1126/sciadv.aar3330

Cannon, K. M., Parman, S. W., & Mustard, J. F. (2017). Primordial clays on Mars formed beneath a steam or supercritical atmosphere. *Nature*, *552*(7683), 88–91. https://doi.org/10.1038/nature24657

Carter, J., Loizeau, D., Mangold, N., Poulet, F., & Bibring, J. P. (2015). Widespread surface weathering on early Mars: A case for a warmer and wetter climate. *Icarus*, *248*, 373–382. https://doi.org/10.1016/j.icarus.2014.11.011

Cloutis, E. A., & Gaffey, M. J. (1991). Spectral-compositional variations in the constituent minerals of mafic and ultramafic assemblages and remote sensing implications. *Earth, Moon, and Planets*, *53*(1), 11–53. https://doi.org/10.1007/bf00116217

Czarnecki, S., Hardgrove, C., Arvidson, R. E., Hughes, M. N., Schmidt, M. E., Henley, T., et al. (2022). Hydration of a clay-rich unit on Mars, comparison of orbital data to rover data. *Journal of Geophysical Research: Planets*, *127*, e2021JE007104. https://doi.org/10.1029/2021JE007104

Czarnecki, S., Hardgrove, C., Gasda, P. J., & Gabriel, T. S. J. (2020). Bulk water in the clay-rich Glen Torridon, Gale Crater, Mars. *51st Lunar and Planetary Science Conference*, 2955.

David, G., Cousin, A., Forni, O., Meslin, P. Y., Dehouck, E., Mangold, N., et al. (2020). Analyses of high-iron sedimentary bedrock and diagenetic features observed with ChemCam at Vera Rubin Ridge, Gale Crater, Mars: Calibration and characterization. *Journal of Geophysical Research: Planets*, *125*(10), e2019JE006314. https://doi.org/10.1029/2019je006314

Dehouck, E., Cousin, A., Mangold, N., Frydenvang, J., Gasnault, O., Forni, O., et al. (2022). Bedrock geochemistry and alteration history of the clay-bearing Glen Torridon region of Gale Crater, Mars. *Journal of Geophysical Research: Planets, 127, e2021JE007103*. https://doi.org/10.1029/2021JE007103

Dehouck, E., Cousin, A., Mangold, N., Frydenvang, J., Gasnault, O., Rapin, W., et al. (2021). Leaving Glen Torridon: Bedrock geochemistry measured by ChemCam en route to the sulfate unit of Gale Crater. In *52nd Lunar and Planetary Science Conference*, 1858.

Deocampo, D. (2015). *Authigenic clay minerals in lacustrine mudstones*, Geological Society of America. https://doi.org/10.1130/2015.2515(03

Edgar, L. A., Fedo, C. M., Gupta, S., Banham, S. G., Fraeman, A. A., Grotzinger, J. P., et al. (2020). A lacustrine paleoenvironment recorded at Vera Rubin Ridge, Gale Crater: Overview of the sedimentology and stratigraphy observed by the Mars Science Laboratory curiosity rover. *Journal of Geophysical Research: Planets*, *125*(3), e2019JE006307. https://doi.org/10.1029/2019je006307

Edgett, K. (2013). MSL Mars Hand Lens Imager camera RDR V1.0, NASA planetary data system. https://doi.org/10.17189/1520292

Edgett, K. S., Yingst, R. A., Ravine, M. A., Caplinger, M. A., Maki, J. N., Ghaemi, F. T., et al. (2012). Curiosity's Mars Hand Lens Imager (MAHLI) investigation. *Space Science Reviews*, *170*(1–4), 259–317. https://doi.org/10.1007/s11214-012-9910-4

Ehlmann, B. L., Mustard, J. F., Fassett, C. I., Schon, S. C., Head, J. W., III, Marais, D. J. D., et al. (2008). Clay minerals in delta deposits and organic preservation potential on Mars. *Nature Geoscience*, *1*(6), 355–358. https://doi.org/10.1038/ngeo207

Ehlmann, B. L., Mustard, J. F., Murchie, S. L., Bibring, J. P., Meunier, A., Fraeman, A. A., & Langevin, Y. (2011). Subsurface water and clay mineral formation during the early history of Mars. *Nature*, *479*(7371), 53–60. https://doi.org/10.1038/nature10582

Fedo, C. M., Bryk, A. B., Edgar, L. A., Bennett, K. A., Fox, V. K., Dietrich, W. E., et al. (2022). Geology and stratigraphic correlation of the Murray and Carolyn Shoemaker formations across the Glen Torridon region, Gale crater, Mars. *Journal of Geophysical Research: Planets*, *127*, e2022JE007408. https://doi.org/10.1029/2022JE007408

Fedo, C. M., Grotzinger, J. P., Bryk, A., Edgar, L. A., Bennett, K., Fox, V., et al. (2020). Ground-based stratigraphic correlation of the Jura and Knockfarrill Hill members of the Murray formation, Gale Crater: Bridging the Vera Rubin Ridge—Glen Torridon divide. In *51st Lunar and Planetary Science Conference*. 2345.

Fox, V. K., Bennett, K. A., Bryk, A., Arvidson, R., Bristow, T., Dehouck, E., et al. (2020). One year in Glen Torridon: Key results from the Mars Science Laboratory curiosity rover exploration of clay-bearing units. In *51st Lunar and Planetary Science Conference*. 2833.

Fox, V. K., Bennett, K. A., Bryk, A., Fedo, C., Dehouck, E., Arvidson, R. E., et al. (2021). Contextualizing CRISM observations of the clay-bearing Glen Torridon region with the Mars Science Laboratory curiosity rover. In *52nd Lunar and Planetary Science Conference*. 2765.

Fraeman, A. A., Arvidson, R. E., Catalano, J. G., Grotzinger, J. P., Morris, R. V., Murchie, S. L., et al. (2013). A hematite-bearing layer in Gale Crater, Mars: Mapping and implications for past aqueous conditions. *Geology*, *41*(10), 1103–1106. https://doi.org/10.1130/g34613.1

Fraeman, A. A., Edgar, L. A., Rampe, E. B., Thompson, L. M., Frydenvang, J., Fedo, C. M., et al. (2020). Evidence for a diagenetic origin of Vera Rubin Ridge, Gale Crater, Mars: Summary and synthesis of Curiosity's exploration campaign. *Journal of Geophysical Research: Planets*, *125*(12), e2020JE006527. https://doi.org/10.1029/2020je006527

Fraeman, A. A., Ehlmann, B. L., Arvidson, R. E., Edwards, C. S., Grotzinger, J. P., Milliken, R. E., et al. (2016). The stratigraphy and evolution of lower Mount Sharp from spectral, morphological, and thermophysical orbital data sets. *Journal of Geophysical Research: Planets*, *121*(9), 1713–1736. https://doi.org/10.1002/2016je005095

Frydenvang, J., Gasda, P. J., Hurowitz, J. A., Grotzinger, J. P., Wiens, R. C., Newsom, H. E., et al. (2017). Diagenetic silica enrichment and late-stage groundwater activity in Gale Crater, Mars. *Geophysical Research Letters*, *44*(10), 4716–4724. https://doi.org/10.1002/2017gl073323

Gasda, P. J., Comellas, J., Essunfeld, A., Das, D., Bryk, A. B., Dehouck, E., et al. (2022). Overview of the morphology and chemistry of diagenetic features in the clay-rich Glen Torridon unit of Gale Crater, Mars. *Journal of Geophysical Research: Planets, 127*, e2021JE007097. https://doi.org/10.1029/2021je007097

Gasda, P. J., Comellas, J., Essunfeld, A., Das, D., Nellessen, M., Dehouck, E., et al. (2021). The chemistry and morphology of diagenetic features in Glen Torridon, Gale Crater. In *52nd Lunar and Planetary Science Conference*. 1271.

Grant, J. A., Wilson, S. A., Mangold, N., Calef, F., & Grotzinger, J. P. (2014). The timing of alluvial activity in Gale Crater, Mars. *Geophysical Research Letters*, *41*(4), 1142–1149. https://doi.org/10.1002/2013gl058909

Grotzinger, J. P., Crisp, J., Vasavada, A. R., Anderson, R. C., Baker, C. J., Barry, R., et al. (2012). Mars Science Laboratory mission and science investigation. *Space Science Reviews*, *170*(1–4), 5–56. https://doi.org/10.1007/s11214-012-9892-2

Grotzinger, J. P., Gupta, S., Malin, M. C., Rubin, D. M., Schieber, J., Siebach, K., et al. (2015). Deposition, exhumation, and paleoclimate of an ancient lake deposit, Gale Crater, Mars. *Science*, *350*(6257), aac7575. https://doi.org/10.1126/science.aac7575

Gutzmer, J., & Beukes, N. J. (1998). Earliest laterites and possible evidence for terrestrial vegetation in the Early Proterozoic. *Geology*, *26*(3), 263–266. https://doi.org/10.1130/0091-7613(1998)026<0263:elapef>2.3.co;2

Haber, J. T., Horgan, B., Fraeman, A. A., Johnson, J. R., Potter-McIntyre, S. L., Bell, J. F., III., et al. (2020). Diagenesis of an ancient lakeshore in Gale Crater, Mars, from Mastcam multispectral images. In *51st Lunar and Planetary Science Conference*. 2112.

He, L., Arvidson, R. E., O'Sullivan, J. A., Morris, R. V., Condus, T., Hughes, M. N., & Powell, K. E. (2022). Surface kinetic temperatures and nontronite single scattering albedo spectra from the Mars Reconnaissance Orbiter CRISM hyperspectral imaging data over Glen Torridon, Gale Crater, Mars. *Journal of Geophysical Research: Planets*, *127*, e2021JE007092. https://doi.org/10.1029/2021JE007092

He, L., Arvidson, R. E., Politte, D. V., Condus, T., & O'Sullivan, J. A. (2019). Retrieving temperatures and single scattering albedos from Martian spectral data using neural networks. In *50th Lunar and Planetary Science Conference*. 2094.

Horgan, B. H. N., Cloutis, E. A., Mann, P., & Bell, J. F. (2014). Near-infrared spectra of ferrous mineral mixtures and methods for their identification in planetary surface spectra. *Icarus*, *234*, 132–154. https://doi.org/10.1016/j.icarus.2014.02.031

Horgan, B. H. N., Johnson, J. R., Fraeman, A. A., Rice, M. S., Seeger, C., Bell, J. F., et al. (2020). Diagenesis of Vera Rubin Ridge, Gale crater, Mars, from Mastcam multispectral images. *Journal of Geophysical Research: Planets*, *125*(11). https://doi.org/10.1029/2019je006322

21699100, 2022, 10, Downloaded from https://agupubs.onlinelibrary.wiley.com/doi/10.1029/2021JE007098 by Cochrane France, Wiley Online Library on [12/04/2023]. See the Terms and Conditions (https://onlinelibrary.wiley.com/terms-and-conditions) on Wiley Online Library for rules of use; OA articles are governed by the applicable Creative Commons License

Hunt, G. R. (1977). Spectral signatures of particulate minerals in the visible and near infrared. *Geophysics*, *42*(3), 501–513. https://doi.org/10.1190/1.1440721

Hurowitz, J. A., Grotzinger, J. P., Fischer, W. W., McLennan, S. M., Milliken, R. E., Stein, N., et al. (2017). Redox stratification of an ancient lake in Gale Crater, Mars. *Science*, *356*(6341). https://doi.org/10.1126/science.aah6849

Johnson, J. R., Bell, J. F., Bender, S., Blaney, D., Cloutis, E., DeFlores, L., et al. (2015). ChemCam passive reflectance spectroscopy of surface materials at the Curiosity landing site, Mars. *Icarus*, *249*, 74–92. https://doi.org/10.1016/j.icarus.2014.02.028

Johnson, J. R., Bell, J. F., Bender, S., Blaney, D., Cloutis, E., Ehlmann, B., et al. (2016). Constraints on iron sulfate and iron oxide mineralogy from ChemCam visible/near-infrared reflectance spectroscopy of Mt. Sharp basal units, Gale Crater, Mars. *American Mineralogist*, *101*(7), 1501–1514. https://doi.org/10.2138/am-2016-5553

Johnson, J. R., Cloutis, E., Wiens, R. C., Maurice, S., Bell, J. F., III, Jacob, S., et al. (2020). Visible/near-infrared reflectance spectra of drill tailings in the Glen Torridon and Greenheugh pediment areas, Gale Crater, Mars. In *AGU Fall meeting*. 680708.

Johnson, J. R., Fraeman, A., Horgan, B. H., Rice, M. S., Wiens, R. C., & Maurice, S. (2019). ChemCam visible/near-infrared spectra of drill tailings and nontronite-bearing rocks in the northern Glen Torridon area, Gale Crater, Mars. In *AGU Fall Meeting*. 489891.

Johnson, J. R., & Ward, J. (2022). MSL ChemCam passive surface spectra bundle. *NASA Planetary Data System*. https://doi.org/10.17189/1520577

Ketzer, J. M., Morad, S., & Amorosi, A. (1999). Predictive diagenetic Clay-mineral distribution in siliciclastic rocks within a sequence stratigraphic framework. In R. H. Worden & S. Morad (Eds.) *Clay Mineral Cements in Sandstones*. https://doi.org/10.1002/9781444304336.ch2

Kinch, K. M., Bell, J. F., Goetz, W., Johnson, J. R., Joseph, J., Madsen, M. B., & Sohl-Dickstein, J. (2015). Dust deposition on the decks of the Mars exploration rovers: 10 years of dust dynamics on the panoramic Camera calibration targets. *Earth and Space Science*, *2*(5), 144–172. https://doi.org/10.1002/2014ea000073

Kokaly, R. F., Clark, R. N., Swayze, G. A., Livo, K. E., Hoefen, T. M., Pearson, N. C., et al. (2017). *USGS spectral Library Version 7* (Report No. 1035; Data Series, p. 61). USGS Publications Warehouse. https://doi.org/10.3133/ds1035

Kronyak, R. E., Kah, L. C., Edgett, K. S., VanBommel, S. J., Thompson, L. M., Wiens, R. C., et al. (2019). Mineral-filled fractures as indicators of multigenerational fluid flow in the Pahrump Hills member of the Murray formation, Gale Crater, Mars. *Earth and Space Science*, *6*(2), 238–265. https://doi.org/10.1029/2018ea000482

L'Haridon, J., Mangold, N., Fraeman, A. A., Johnson, J. R., Cousin, A., Rapin, W., et al. (2020). Iron mobility during diagenesis at Vera Rubin Ridge, Gale Crater, Mars. *Journal of Geophysical Research: Planets*, *125*(11). https://doi.org/10.1029/2019je006299

Malin, M. (2013). MSL Mars mast camera RDR V1.0, NASA planetary data system. https://doi.org/10.17189/1520328

Malin, M. C., & Edgett, K. S. (2000). Sedimentary rocks of early Mars. *Science*, *290*(5498), 1927–1937. https://doi.org/10.1126/science.290.5498.1927

Malin, M. C., Ravine, M. A., Caplinger, M. A., Ghaemi, F. T., Schaffner, J. A., Maki, J. N., et al. (2017). The Mars Science Laboratory (MSL) mast cameras and descent imager: Investigation and instrument descriptions. *Earth and Space Science*, *4*(8), 506–539. https://doi.org/10.1002/2016ea000252

Martin, P. E., Farley, K. A., Baker, M. B., Malespin, C. A., Schwenzer, S. P., Cohen, B. A., et al. (2017). A two-step K-Ar experiment on Mars: Dating the diagenetic formation of Jarosite from Amazonian groundwaters. *Journal of Geophysical Research: Planets*, *122*(12), 2803–2818. https://doi.org/10.1002/2017je005445

Maurice, S., Wiens, R. C., Saccoccio, M., Barraclough, B., Gasnault, O., Forni, O., et al. (2012). The ChemCam instrument suite on the Mars Science Laboratory (MSL) rover: Science objectives and mast unit description. *Space Science Reviews*, *170*(1–4), 95–166. https://doi.org/10.1007/s11214-012-9912-2

McAdam, A. C., Sutter, B., Archer, P. D., Franz, H. B., Wong, G. M., Lewis, J. M. T., et al. (2020). Constraints on the mineralogy and geochemistry of Vera Rubin Ridge, Gale Crater, Mars, from Mars Science Laboratory sample analysis at Mars evolved gas analyses. *Journal of Geophysical Research: Planets*, *125*(11). https://doi.org/10.1029/2019je006309

McEwen, A., (2007). Mars reconnaissance orbiter high resolution imaging science experiment, reduced data record, MRO-M-HIRISE-3-RDR-V1.1. *NASA planetary data system*. https://doi.org/10.17189/1520303

McKinley, J., Worden, R., & Ruffell, A. (2002). *Smectite in sandstones: A review of the controls on occurrence and behaviour during diagenesis* (pp. 109–128). International Association of Sedimentologists Special Publications. https://doi.org/10.1002/9781444304336.ch5

Michalski, J. R., Cuadros, J., Niles, P. B., Parnell, J., Rogers, A. D., & Wright, S. P. (2013). Groundwater activity on Mars and implications for a deep biosphere. *Nature Geoscience*, *6*(2), 133–138. https://doi.org/10.1038/ngeo1706

Millan, M., Williams, A. J., McAdam, A., Eigenbrode, J. L., Freissinet, C., Glavin, D. P., et al. (2021). Organic molecules revealed in Glen Torridon by the SAM instrument. *52nd Lunar and Planetary Science Conference*, 2021–2039.

Milliken, R. E., Grotzinger, J. P., & Thomson, B. J. (2010). Paleoclimate of Mars as captured by the stratigraphic record in Gale Crater. *Geophysical Research Letters*, *37*(4). https://doi.org/10.1029/2009gl041870

Minitti, M. E., Rivera-Hernández, F., Bennett, K. A., Gupta, S., & Wiens, R. C. (2021). Rock textures and grain sizes in the Glen Torridon region (Gale Crater, Mars) observed by the Mars Hand Lens Imager (MAHLI) and ChemCam. In *52nd Lunar and Planetary Science Conference 2021*. 2435.

Morris, R. V., Agresti, D. G., Lauer, H. V., Newcomb, J. A., Shelfer, T. D., & Murali, A. V. (1989). Evidence for pigmentary hematite on Mars based on optical, magnetic, and Mossbauer studies of superparamagnetic (nanocrystalline) hematite. *Journal of Geophysical Research*, *94*(B3), 2760–2778. https://doi.org/10.1029/jb094ib03p02760

Morris, R. V., Lauer, H. V., Lawson, C. A., Gibson, E. K., Nace, G. A., & Stewart, C. (1985). Spectral and other physicochemical properties of submicron powders of hematite (α-Fe_2O_3), maghemite (γ-Fe_2O_3), magnetite (Fe_3O_4), goethite (α-FeOOH), and lepidocrocite (γ-FeOOH). *Journal of Geophysical Research*, *90*(B4), 3126–3144. https://doi.org/10.1029/jb090ib04p03126

Murchie, S., Arvidson, R., Bedini, P., Beisser, K., Bibring, J.-P., Bishop, J., et al. (2007). Compact reconnaissance imaging spectrometer for Mars (CRISM) on Mars reconnaissance orbiter (MRO). *Journal of Geophysical Research*, *112*(E5), E05S03. https://doi.org/10.1029/2006je002682

Nachon, M., Mangold, N., Forni, O., Kah, L. C., Cousin, A., Wiens, R. C., et al. (2017). Chemistry of diagenetic features analyzed by ChemCam at Pahrump Hills, Gale Crater, Mars. *Icarus*, *281*, 121–136. https://doi.org/10.1016/j.icarus.2016.08.026

Nesbitt, H. W., & Young, G. M. (1982). Early Proterozoic climates and plate motions inferred from major element chemistry of lutites. *Nature*, *299*(5885), 715–717. https://doi.org/10.1038/299715a0

Newsom, H. E. (1980). Hydrothermal alteration of impact melt sheets with implications for Mars. *Icarus*, *44*(1), 207–216. https://doi.org/10.1016/0019-1035(80)90066-4

Noe Dobrea, E. Z., Bishop, J. L., McKeown, N. K., Fu, R., Rossi, C. M., Michalski, J. R., et al. (2010). Mineralogy and stratigraphy of phyllosilicate-bearing and dark mantling units in the greater Mawrth Vallis/West Arabia Terra area: Constraints on geological origin. *Journal of Geophysical Research*, *115*(E7), E00D19. https://doi.org/10.1029/2009je003351

21699100, 2022, 10, Downloaded from https://agupubs.onlinelibrary.wiley.com/doi/10.1029/2021JE007098 by Cochrane France, Wiley Online Library on [12/04/2023]. See the Terms and Conditions (https://onlinelibrary.wiley.com/terms-and-conditions) on Wiley Online Library for rules of use; OA articles are governed by the applicable Creative Commons License

O'Connell-Cooper, C. D., Gellert, R., & Thompson, L. M. (2022). Statistical analysis of APXS-derived chemistry of the clay-bearing Glen Torridon region and Mount Sharp group, Gale Crater, Mars. *Journal of Geophysical Research: Planets*, *127*, e2021JE007177. https://doi.org/10.1029/2021JE007177

O'Connell-Cooper, C. D., Thompson, L. M., Gellert, R., Spray, J. G., Boyd, N. I., Berger, J., et al. (2021). APXS geochemistry of the fracture Intermediate Unit (fIU)—Its relationship to underlying Glen Torridon units and overlying pediment rocks at the Greenheugh unconformity. In *52nd Lunar and Planetary Science Conference*.

Pieters, C. M. (1983). Strength of mineral absorption features in the transmitted component of near-infrared reflected light: First results from RELAB. *Journal of Geophysical Research*, *88*(B11), 9534–9544. https://doi.org/10.1029/JB088iB11p09534

Rampe, E. B., Blake, D. F., Bristow, T. F., Ming, D. W., Vaniman, D. T., Morris, R. V., et al. (2020). Mineralogy and geochemistry of sedimentary rocks and Aeolian sediments in Gale Crater, Mars: A review after six Earth years of exploration with curiosity. *Geochemistry*, *80*(2), 125605. https://doi.org/10.1016/j.chemer.2020.125605

Rampe, E. B., Bristow, T. F., Morris, R. V., Morrison, S. M., Achilles, C. N., Ming, D. W., et al. (2020). Mineralogy of Vera Rubin Ridge from the Mars Science Laboratory CheMin instrument. *Journal of Geophysical Research: Planets*, *125*(9). https://doi.org/10.1029/2019je006306

Rampe, E. B., Ming, D. W., Blake, D. F., Bristow, T. F., Chipera, S. J., Grotzinger, J. P., et al. (2017). Mineralogy of an ancient lacustrine mudstone succession from the Murray formation, Gale Crater, Mars. *Earth and Planetary Science Letters*, *471*, 172–185. https://doi.org/10.1016/j.epsl.2017.04.021

Rapin, W., Ehlmann, B. L., Dromart, G., Schieber, J., Thomas, N. H., Fischer, W. W., et al. (2019). An interval of high salinity in ancient Gale Crater Lake on Mars. *Nature Geoscience*, *12*(11), 889–895. https://doi.org/10.1038/s41561-019-0458-8

Rivera-Hernández, F., Sumner, D. Y., Mangold, N., Banham, S. G., Edgett, K. S., Fedo, C. M., et al. (2020). Grain size variations in the Murray formation: Stratigraphic evidence for changing depositional environments in Gale Crater, Mars. *Journal of Geophysical Research: Planets*, *125*(2), e2019JE006230. https://doi.org/10.1029/2019je006230

Rivera-Hernández, F., Sumner, D. Y., Minitti, M., Bennett, K. A., Bryk, A., Edgett, K. S., et al. (2020). Grain size and facies variations in Glen Torridon (Gale Crater, Mars): Perspective from MAHLI, Mastcam, and ChemCam LIBS data. In *51st Lunar and Planetary Science Conference*. 2814.

Robinson, M., Collins, C., Leger, P., Kim, W., Carsten, J., Tompkins, V., et al. (2013). Test and validation of the Mars Science Laboratory robotic arm. In *2013 8th International Conference on System of Systems Engineering* (pp. 184–189). https://doi.org/10.1109/sysose.2013.6575264

Rudolph, A., & Johnson, J. (2022). *Data for: The distribution of clay minerals and their impact on diagenesis in Glen Torridon, Gale Crater, Mars*. Mendeley Data, V1. https://doi.org/10.17632/6g3c3g6b9z.1

Sherman, D. (1990). *Crystal chemistry, electronic structures, and spectra of Fe sites in clay minerals*. American Chemical Society Symposium Series. Chp. 15.

Siebach, K. L., Baker, M. B., Grotzinger, J. P., McLennan, S. M., Gellert, R., Thompson, L. M., & Hurowitz, J. A. (2017). Sorting out compositional trends in sedimentary rocks of the Bradbury group (Aeolis Palus), Gale Crater, Mars. *Journal of Geophysical Research: Planets*, *122*(2), 295–328. https://doi.org/10.1002/2016je005195

Stack, K. M., Grotzinger, J. P., Kah, L. C., Schmidt, M. E., Mangold, N., Edgett, K. S., et al. (2014). Diagenetic origin of nodules in the sheepbed member, Yellowknife Bay formation, Gale Crater, Mars. *Journal of Geophysical Research: Planets*, *119*(7), 1637–1664. https://doi.org/10.1002/2014je004617

Stein, N., Grotzinger, J. P., Schieber, J., Mangold, N., Hallet, B., Newsom, H., et al. (2018). Desiccation cracks provide evidence of lake drying on Mars, Sutton Island member, Murray formation, Gale Crater. *Geology*, *46*(6), 515–518. https://doi.org/10.1130/g40005.1

Summons, R. E., Amend, J. P., Bish, D., Buick, R., Cody, G. D., Marais, D. J. D., et al. (2011). Preservation of Martian organic and environmental records: Final report of the Mars biosignature working group. *Astrobiology*, *11*(2), 157–181. https://doi.org/10.1089/ast.2010.0506

Sun, V. Z., Stack, K. M., Kah, L. C., Thompson, L., Fischer, W., Williams, A. J., et al. (2019). Late-stage diagenetic concretions in the Murray formation, Gale Crater, Mars. *Icarus*, *321*, 866–890. https://doi.org/10.1016/j.icarus.2018.12.030

Sutter, B., McAdam, A. C., Mahaffy, P. R., Ming, D. W., Edgett, K. S., Rampe, E. B., et al. (2017). Evolved gas analyses of sedimentary rocks and Aeolian sediment in Gale Crater, Mars: Results of the Curiosity rover's sample analysis at Mars instrument from Yellowknife Bay to the Namib dune. *Journal of Geophysical Research: Planets*, *122*(12), 2574–2609. https://doi.org/10.1002/2016je005225

Tardy, Y. (1992). Chapter 15 Diversity and terminology of lateritic profiles. *Developments in Earth Surface Processes*, *2*, 379–405. https://doi.org/10.1016/b978-0-444-89198-3.50020-9

Thompson, L. M., O'Connell-Cooper, C., Berger, J. A., & Yen, A., (2022). Alteration at the base of the Siccar Point unconformity and further evidence for an alkaline provenance at Gale crater: Exploration of the Mount Sharp group, Greenheugh pediment cap rock contact with APXS. *Journal of Geophysical Research: Planets*, *127*, e2021JE007178. https://doi.org/10.1029/2021JE07178

Thompson, L. M., Yen, A. S., O'Connell-Cooper, C. D., Berger, J. A., Gellert, R., McCraig, M. A., et al. (2021). APXS-Derived compositions of Greenheugh pediment capping rock and immediately underlying Murray formation: Implications. In *52nd Lunar and Planetary Science Conference*. 2411.

Thorpe, M., Bristow, T. F., Rampe, E. B., Grotzinger, J. P., Fox, V. K., Bennett, K. A., et al. (2020). Glen Torridon mineralogy and the sedimentary history of the clay mineral bearing unit. In *51st Lunar and Planetary Science Conference*. 1524.

Thorpe, M. T., Bristow, T. F., Rampe, E. B., Grotzinger, J. P., Fox, V. K., Bennett, K. A., et al. (2021). The mineralogy and sedimentary history of the Glen Torridon region, Gale Crater, Mars. In *52nd Lunar and Planetary Science Conference*. 1519.

Thorpe, M. T., Bristow, T. F., Rampe, E. B., Tosca, N. J., Grotzinger, J. P., Bennett, K. A., et al. (2022). Mars Science Laboratory CheMin data from the Glen Torridon region and the significance of lake-groundwater interactions in interpreting mineralogy and sedimentary history. *Journal of Geophysical Research: Planets*, *127*, e2021JE007099. https://doi.org/10.1029/2021JE007099

Treiman, A. H., Morris, R. V., Agresti, D. G., Graff, T. G., Achilles, C. N., Rampe, E. B., et al. (2014). Ferrian Saponite from the Santa Monica Mountains (California, U.S.A., Earth): Characterization as an analog for clay minerals on Mars with application to Yellowknife Bay in Gale Crater. *American Mineralogist*, *99*(11–12), 2234–2250. https://doi.org/10.2138/am-2014-4763

Vaniman, D. T., Bish, D. L., Ming, D. W., Bristow, T. F., Morris, R. V., Blake, D. F., et al. (2014). Mineralogy of a mudstone at Yellowknife Bay, Gale Crater, Mars. *Science*, *343*(6169). https://doi.org/10.1126/science.1243480

Velde, B. (Ed.), (1995). *Origin and mineralogy of clays*, Springer Berlin Heidelberg. https://doi.org/10.1007/978-3-662-12648-6

Wattel-Koekkoek, E. J. W., Buurman, P., van der Plicht, J., Wattel, E., & Van Breemen, N. V. (2003). Mean residence time of soil organic matter associated with kaolinite and smectite.pdf. *European Journal of Soil Science*, *54*(2), 269–278. https://doi.org/10.1046/j.1365-2389.2003.00512.x

Wellington, D. F., Bell, J. F., Johnson, J. R., Kinch, K. M., Rice, M. S., Godber, A., et al. (2017). Visible to near-infrared MSL/Mastcam multispectral imaging: Initial results from select high-interest science targets within Gale Crater, Mars. *American Mineralogist*, *102*(6), 1202–1217. https://doi.org/10.2138/am-2017-5760ccby

21699100, 2022, 10, Downloaded from https://agupubs.onlinelibrary.wiley.com/doi/10.1029/2021JE007098 by Cochrane France, Wiley Online Library on [12/04/2023]. See the Terms and Conditions (https://onlinelibrary.wiley.com/terms-and-conditions) on Wiley Online Library for rules of use; OA articles are governed by the applicable Creative Commons License

Wiens, R. C., Maurice, S., Barraclough, B., Saccoccio, M., Barkley, W. C., Bell, J. F., et al. (2012). The ChemCam instrument suite on the Mars Science Laboratory (MSL) rover: Body unit and combined system tests. *Space Science Reviews*, *170*(1–4), 167–227. https://doi.org/10.1007/s11214-012-9902-4

Worden, R. H., & Morad, S. (1999). Clay minerals in sandstones: Controls on formation, distribution and evolution. In *Clay mineral cements in sandstones* In (Eds. R. H. Worden & S. Morad (Eds.),). https://doi.org/10.1002/9781444304336.ch1

Yen, A. S., Ming, D. W., Vaniman, D. T., Gellert, R., Blake, D. F., Morris, R. V., et al. (2017). Multiple stages of aqueous alteration along fractures in mudstone and sandstone strata in Gale Crater, Mars. *Earth and Planetary Science Letters*, *471*, 186–198. https://doi.org/10.1016/j.epsl.2017.04.033

21699100, 2022, 10, Downloaded from https://agupubs.onlinelibrary.wiley.com/doi/10.1029/2021JE007098 by Cochrane France, Wiley Online Library on [12/04/2023]. See the Terms and Conditions (https://onlinelibrary.wiley.com/terms-and-conditions) on Wiley Online Library for rules of use; OA articles are governed by the applicable Creative Commons License